Handbook of Workability and Process Design
G.E. Dieter, H.A. Kuhn, and S.L. Semiatin, editors, p 172-187
DOI:10.1361/hwpd2003p172

Chapter 12

Workability Theory and Application in Bulk Forming Processes*

Howard A. Kuhn, Consultant

WORKABILITY, as described in previous chapters, is not merely a property of a material but a characteristic of the material/process system. The role of the material is measured by a simple test or tests and should be expressed in a quantitative form that is applicable universally. This measure is taken to be a basic property of the material composition and structure, and it reflects the macroscopic outcome of the micromechanisms of plastic flow perturbed by such inhomogeneities as voids, inclusions, and grain boundaries. Such phenomena are dependent not only on the material structure but also on the process parameters (strain rate and temperature), which define the role of the process in determining workability.

The micromechanisms of ductile fracture in bulk forming processes are strongly influenced by the stress and strain environment imposed by the process. As shown in Fig. 10 of Chapter 2, overall measure of strain to fracture can be related to an overall value of hydrostatic stress in the material during processing. In the spectrum of processes (extrusion, rolling, forging, and wire drawing), the average hydrostatic stress becomes increasingly tensile, and the strain to fracture progressively decreases. Within each of these processes, however, the stress and strain states can be considered on a localized basis in the specific regions in which fractures initiate. These localized conditions are controlled by the geometry of the workpiece, die design, and friction at the die/workpiece interface. These three factors, in addition to the strain rate and temperature parameters already mentioned, embody the role of the process in determining workability.

This article focuses on the effects of mechanical plasticity on workability; that is, process control of localized stress and strain conditions to enhance workability. First, the nature of local stress and strain states in bulk forming processes is described, leading to a classification scheme that facilitates the application of workability concepts. This defines testing procedures and specific process measurements for an experimental approach to workability evaluation. Theoretical models and fracture criteria are then described and compared with experimental results. Finally, the application of workability concepts to forging, rolling, and extrusion processes is discussed.

Stress and Strain States

Forging, extrusion, and rolling processes generally are considered to involve the application of compressive force to material to impart a change in shape and dimensions. On close examination, however, it is clear that deformation resulting from the applied load causes secondary stress and strain states that vary from point to point throughout the deforming workpiece. These stress and strain states may include tension, so fracture can occur at certain locations in a material even though the primary (applied) load is compressive.

To explore this possibility further, it is useful to review briefly the von Mises yield criterion, which is the foundation of plasticity theory for isotropic materials. It gives the relationships between normal and shear stress components at yielding. From this, relationships between stress and strain components are derived:

$$\varepsilon_1 = \lambda\left[\sigma_1 - \frac{1}{2}\sigma_2 - \frac{1}{2}\sigma_3\right]$$
$$\varepsilon_2 = \lambda\left[\sigma_2 - \frac{1}{2}\sigma_3 - \frac{1}{2}\sigma_1\right]$$
$$\varepsilon_3 = \lambda\left[\sigma_3 - \frac{1}{2}\sigma_1 - \frac{1}{2}\sigma_2\right] \quad \text{(Eq 1)}$$

where ε denotes strain, σ denotes stress, and the subscripts 1, 2, and 3 designate the three directions in an orthogonal coordinate system. Here, λ is a proportionality factor dependent on the deformation history and flow stress curve of the material. The resulting strain in a given direction is affected by the stress in all three coordinate directions. In addition, these relationships satisfy the volume constancy condition, $\varepsilon_1 + \varepsilon_2 + \varepsilon_3 = 0$.

To illustrate these relationships, it is useful to consider a two-dimensional case of plane stress, $\sigma_3 = 0$:

$$\varepsilon_1 = \lambda\left[\sigma_1 - \frac{1}{2}\sigma_2\right]$$
$$\varepsilon_2 = \lambda\left[\sigma_2 - \frac{1}{2}\sigma_1\right] \quad \text{(Eq 2)}$$

Referring to Fig. 1 and Eq 2, a reduction in thickness (compressive strain in the 2-direction)

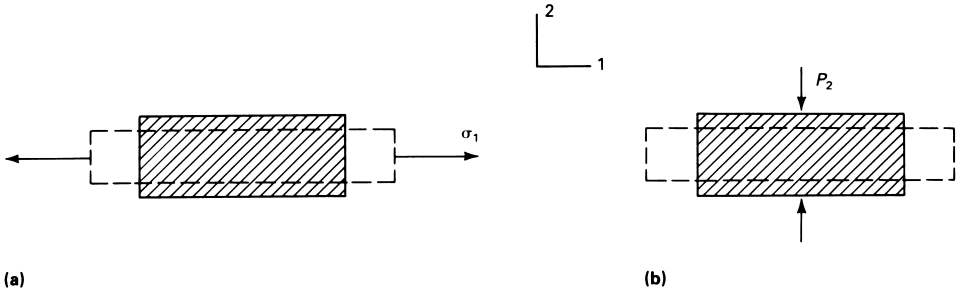

Fig. 1 Similarity of deformation under (a) horizontal tension and (b) vertical compression

*This article is revised from Howard A. Kuhn, Workability Theory and Application in Bulk Forming Processes, *Forming and Forging*, Vol 14, *ASM Handbook,* ASM International, 1988, p 388–404.

can be accomplished either by a compressive stress, P_2 (or $-\sigma_2$), or by a tensile stress, σ_1. Although the nature of the deformation is the same in both cases, accomplishing that deformation in the latter case could risk fracture because it involves a tensile stress.

For more general cases, Eq 2 can be rearranged to determine the following stresses:

$$\sigma_1 = \frac{4}{3\lambda}\left[\varepsilon_1 + \frac{1}{2}\varepsilon_2\right] = \frac{4}{3\lambda}\varepsilon_1\left[1 + \frac{1}{2}\frac{\varepsilon_2}{\varepsilon_1}\right]$$
$$\sigma_2 = \frac{4}{3\lambda}\left[\varepsilon_2 + \frac{1}{2}\varepsilon_1\right] = \frac{4}{3\lambda}\varepsilon_1\left[\frac{1}{2} + \frac{\varepsilon_2}{\varepsilon_1}\right]$$
$$\sigma_3 = 0 \qquad \text{(Eq 3)}$$

Therefore, the stresses depend on the localized strains ε_1 and ε_2 that result from metal flow. Equation 3 is a more convenient representation of plasticity relationships for workability study.

For example, the cylindrical surface of a compression test undergoes various combinations of axial and circumferential strains, depending on the aspect ratio and the friction at the die contact surfaces (Fig. 2). When no friction exists, the ratio of circumferential strain to axial strain is $\varepsilon_1/\varepsilon_2 = -½$. According to the first part of Eq 3, $\sigma_1 = 0$ for this case. The deformation in this case is referred to as homogeneous compression, because the only stress acting is σ_2 and it is uniform throughout the specimen. Therefore, the homogeneous compression test is suitable for measuring flow stress.

When friction exists at the die contact surfaces, material at these surfaces is constrained from moving outward, while material at the midplane is not constrained. As a result, bulging occurs, as shown in Fig. 2(a). Under these conditions, the circumferential strain ε_1 (>0) increases, and the localized axial compressive strain ε_2 (<0) decreases. From Eq 3 as $\varepsilon_1/\varepsilon_2$ becomes more negative ($<-½$), σ_1 becomes more positive. Therefore, increasing bulging due to friction during the compression of a cylinder increases the secondary tensile stress σ_1 and enhances the likelihood of fracture.

Similarly, at the edges of bars during rolling (Fig. 3), the elongation strain ε_1 is determined by the overall reduction in area. The localized compressive vertical strain ε_2, however, depends on the shape of the edge. Greater convexity and sharpness of the edge decrease the compressive vertical strain for a given reduction, which, from the first part of Eq 3, increases the secondary tensile stress σ_1 at the edge. Therefore, edge cracking during rolling is also due to secondary stress states.

More complex cases of the same type of secondary tensile stress states occur in forging (Fig. 4). During the forging of a hub shape, for example, the top surface of the hub is subjected to biaxial tension because of friction during flow around the die radius (Fig. 4a). This is identical to the conditions present at the nose of a billet that is being extruded or rolled. Similarly, during forging, the top surface of a rib undergoes tensile strain in the direction of curvature, and essentially no strain occurs along the length direction of the rib (Fig. 4b). In both cases, localized secondary tensile stresses are generated that may cause fracture. These stresses can be calculated from measured strain values using Eq 3.

Figures 2 to 4 show examples of plane stress, with the stress normal to the free surface being zero. Other regions of workpieces in bulk deformation processes, however, are subjected to three-dimensional stress states. For example, material at the die contact surfaces in forging, extrusion, and rolling (Fig. 5) is subjected to strains ε_1 and ε_2 in the plane of the surface, as in Fig. 2 to 4. In Fig. 5, however, this surface is also acted upon by pressure P_3 normal to the plane. Similarly, at internal locations of the workpieces in such processes as forging or wire drawing (Fig. 6), a material element of the central longitudinal plane is subjected to strains ε_1 and ε_2 and stress normal to the plane.

In Fig. 5 and 6, the material element can be thought of as the plane-stress elements in Fig. 2 to 4 with σ_3 acting normal to the plane. If ε_1 and ε_2 are taken to be the strains in this plane, then Eq 3 becomes:

$$\sigma_1 = \frac{4}{3\lambda}\left[\varepsilon_1 + \frac{1}{2}\varepsilon_2\right] + \sigma_3$$
$$\sigma_2 = \frac{4}{3\lambda}\left[\varepsilon_2 + \frac{1}{2}\varepsilon_1\right] + \sigma_3$$
$$\sigma_3 = \sigma_3$$

In other words, for the same deformation (that is, the same values of ε_1 and ε_2 as in Fig. 2 to 4), the stresses σ_1 and σ_2 in Eq 3 are biased by σ_3. The stress normal to the surface, then, increases the hydrostatic stress component of the stress state by σ_3. This reflects the basic concept that hydrostatic stress does not affect yielding or plastic deformation. As shown in Fig. 10 of Chapter 2, "Bulk Working Behavior of Metals," however, the hydrostatic stress has a significant effect on fracture. In Fig. 5, the compressive stress (die pressure) P_3 would increase the strains at fracture, but in Fig. 6 the internal stress σ_3 may be tensile and decrease the strains at fracture.

The preceding discussion of stress and strain states in various regions of workpieces suggests a convenient method of classifying cracking defects. Figures 2 to 4 in this article illustrate the locations at which free surface cracks occur in forging and rolling, as well as at the nose ends of billets in extrusion or rolling. Figure 5 in this article shows examples of circumstances in which contact surface cracking occurs—for example, the fir tree defect in extrusion or the longitudinal surface cracks in rolled plates.

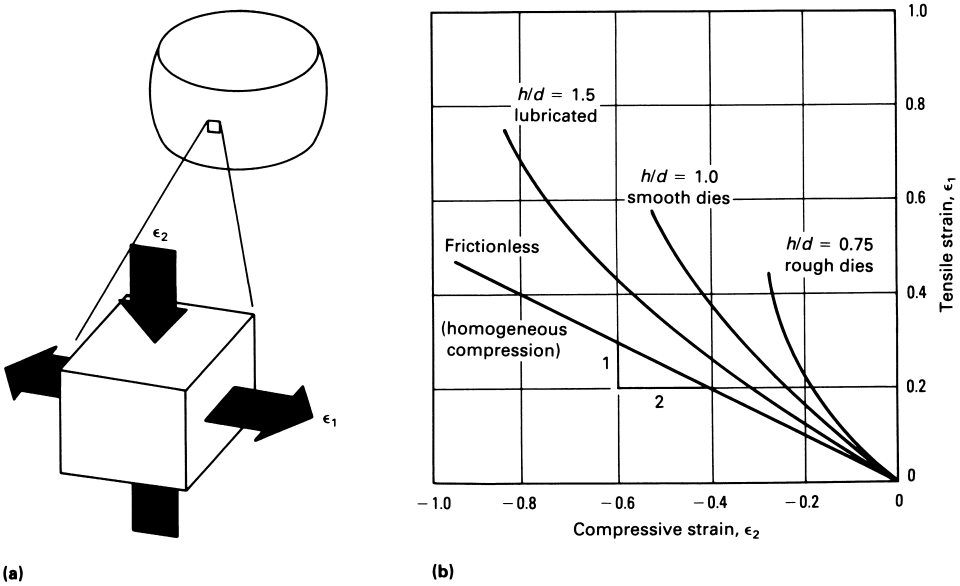

Fig. 2 Localized strains on (a) the bulging cylindrical surface of an upset test and (b) their variation with aspect ratio and friction conditions. Source: Ref 1

Empirical Criterion of Fracture

The stress and strain environments described in the previous section in this article suggest that a workability test should be capable of subjecting the material to a variety of surface strain combinations. A capability for testing under superimposed normal stress would also be desirable.

When considering workability tests, it is important to recognize that fractures initiate in localized regions where interaction between the stress and strain states and the material structure reaches a critical level. Orientation, shape, and volume fraction of inclusions and other inhomogeneities have a dominant effect on the fracture process. Therefore, it is critically important that workability test specimens contain material hav-

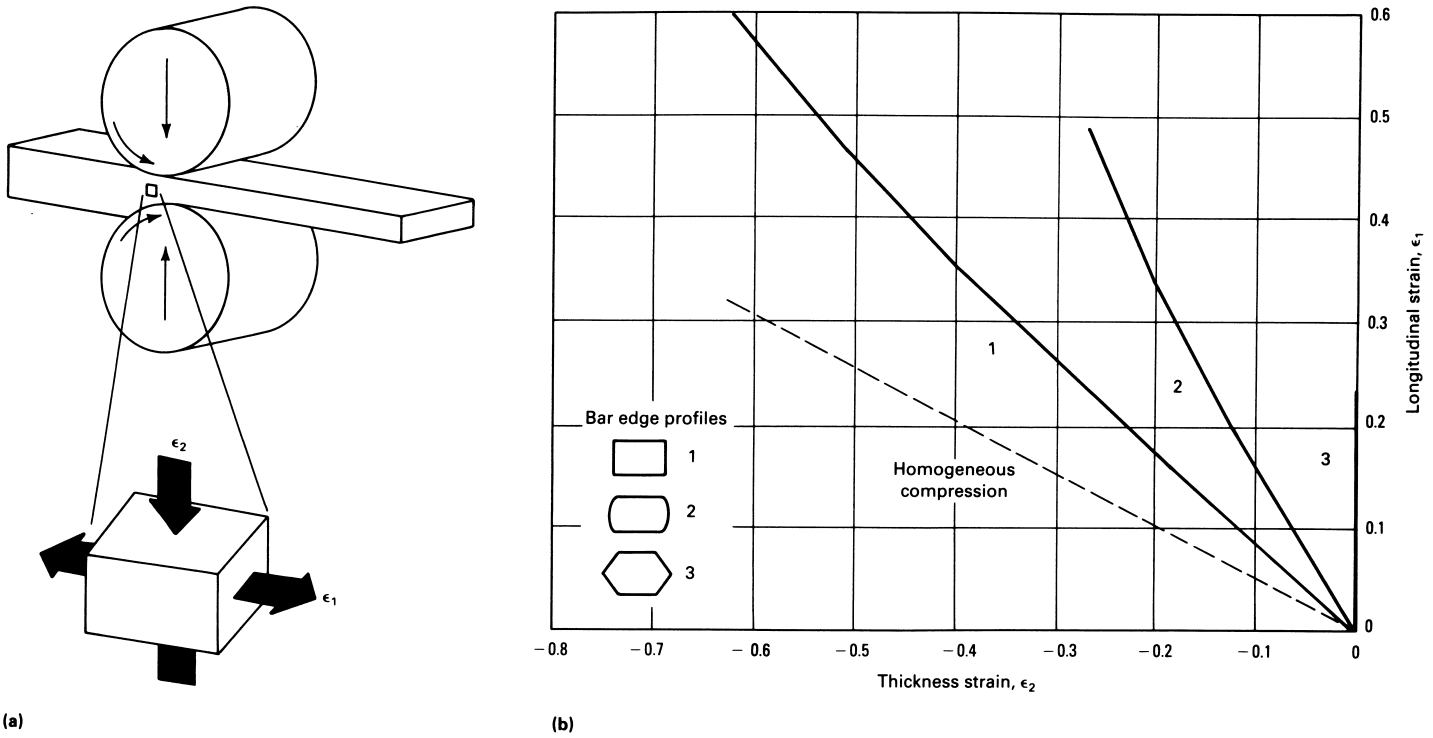

Fig. 3 Localized strains at the edges of bars during (a) rolling and (b) their variation with edge profile. Source: Ref 2

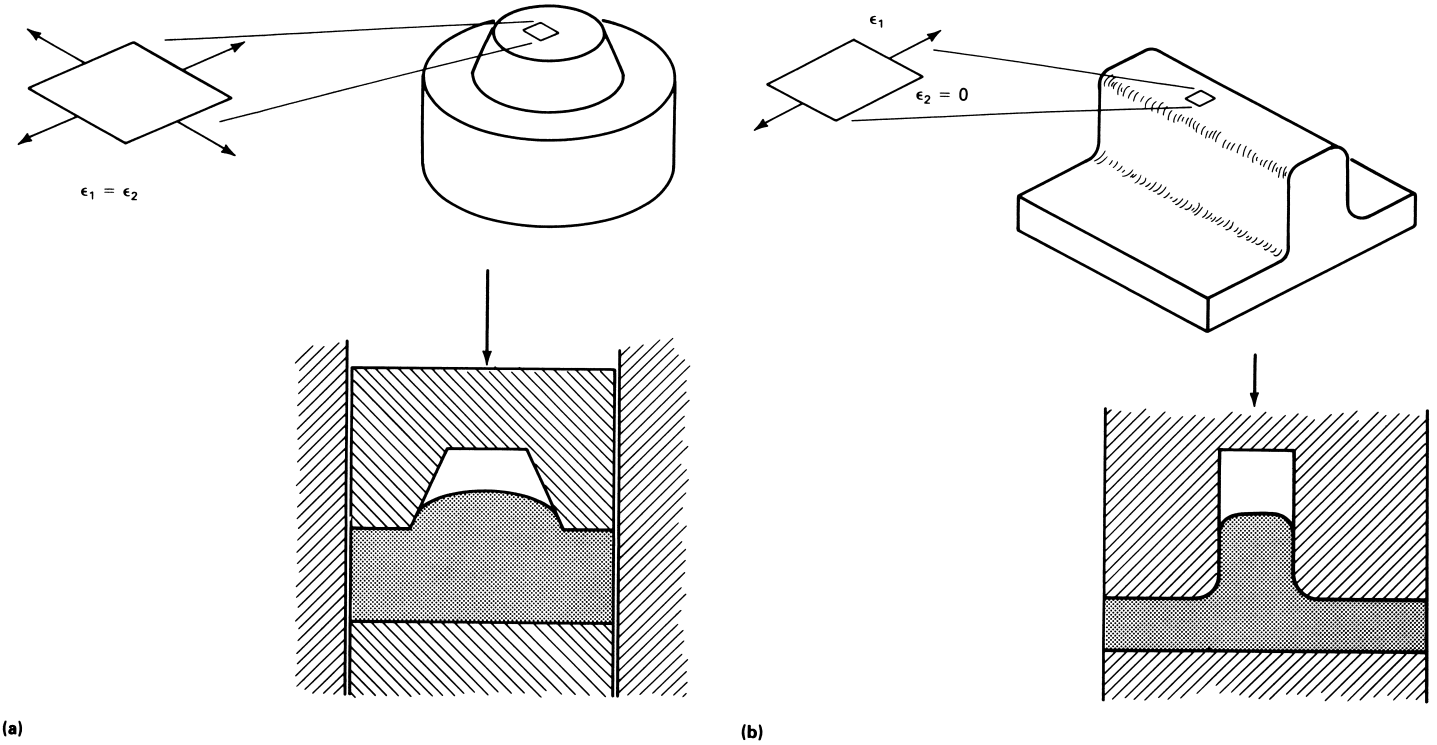

Fig. 4 Strains at the free surfaces of forgings. (a) Axisymmetric hub. (b) Rib-web forging

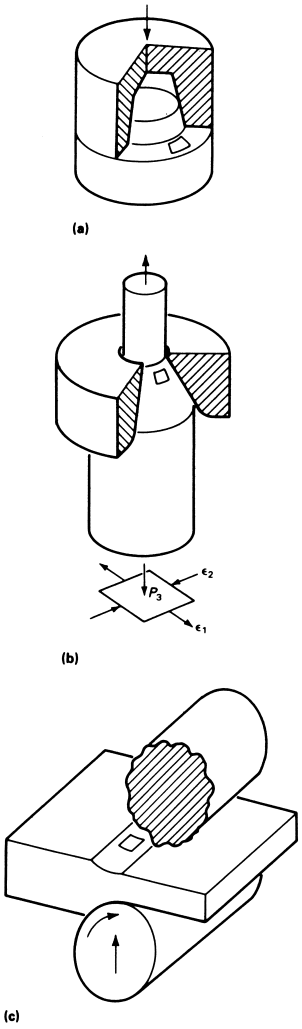

Fig. 5 An element of material at the die contact surfaces during (a) forging, (b) drawing or extrusion, and (c) rolling

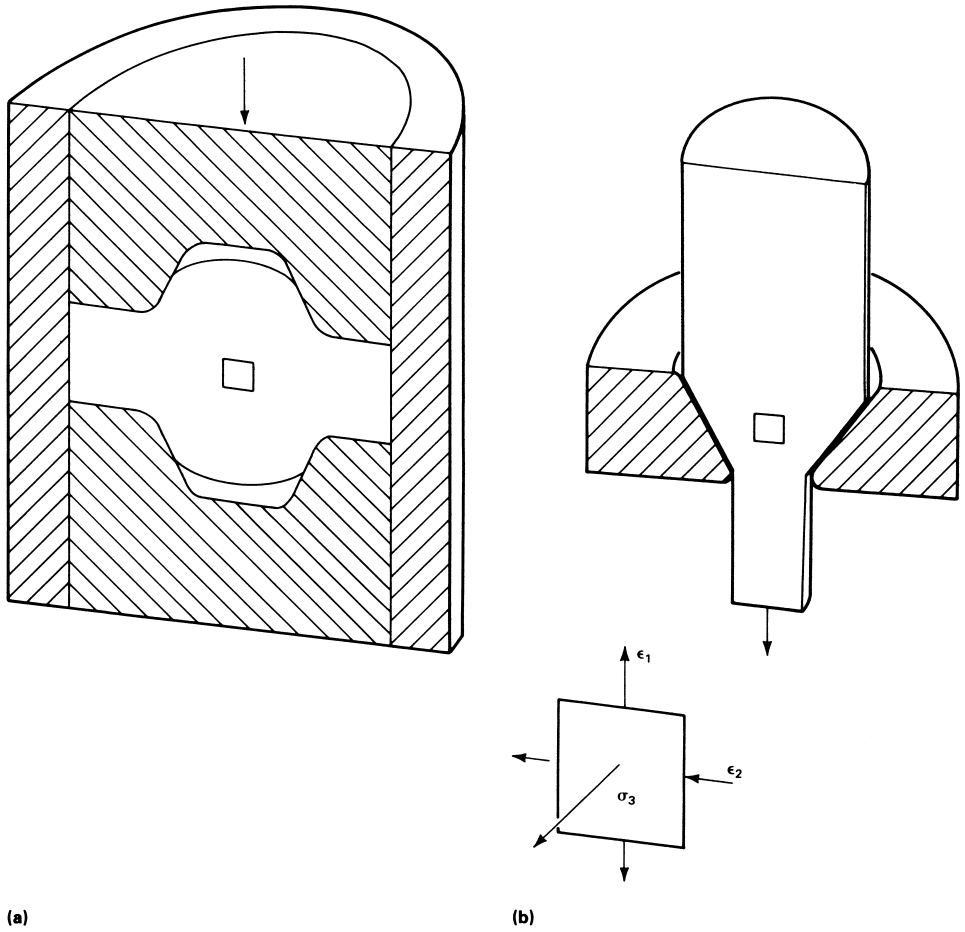

Fig. 6 An element of material at the center of a forging undergoing (a) double extrusion and (b) at the center of wire being drawn. The element undergoes strains ε_1, and ε_2, as in Fig. 2 to 4, with stress σ_3 normal to the 1–2 plane.

ing the same microstructural features as the material in the localized, potential fracture regions of the actual process.

Specifically, when evaluating a workpiece for surface fractures, specimen surfaces must contain the as-received surface of the workpiece under consideration because it may contain laps, seams, a decarburized layer, and so on, which affect fracture initiation. By the same argument, evaluation of material for internal fractures such as central burst must involve test specimens taken from the middle of the workpiece, where, for example, segregation of second phases may have occurred. Because of possible anisotropy effects, orientation of the critical stresses with respect to any inclusion alignment must be the same in the test specimens as it is in the actual process and material of interest.

The compression test has become a standard for workability evaluation. As shown in Fig. 2, a range of strain combinations can be developed at the cylindrical free surface simply by altering

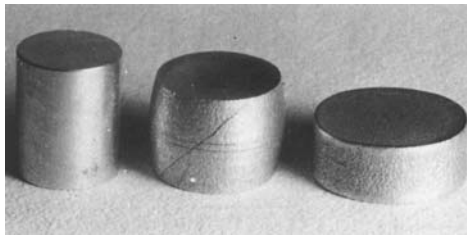

Fig. 7 Compression tests on 2024-T35 aluminum alloy. Left to right: undeformed specimen, compression with friction (cracked), compression without friction (no cracks)

friction and geometry conditions. The influence of friction and consequent bulging on circumferential tensile stress development is clearly shown in Fig. 7. Compression with friction produces circumferential tension that leads to fracture, while frictionless compression prevents barreling, tension, and cracking as described in Fig. 2 and Eq 3.

Alterations of the compression test geometry have been devised to extend the range of surface strains available toward the vertical, tensile

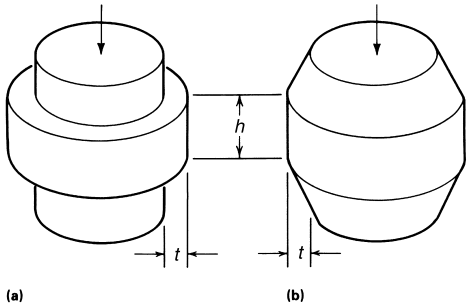

Fig. 8 (a) Flanged and (b) tapered prebulged compression test specimens. Lateral spread of interior material under compression expands the rim circumferentially while little axial compression is applied (see Fig. 9).

strain axis, ε_1 (Ref 3). Test specimens are artificially prebulged by machining a taper or a flange on the cylinders (Fig. 8). Compression then causes lateral spread of the interior material, which expands the rim circumferentially while applying little axial compression to the rim. Therefore, the tapered and flanged upset test specimens provide strain states consisting of

small compressive strain components. Each combination of height, h, and thickness, t, gives a different ratio of tensile to compressive strain. The strain states developed at the surfaces of straight, tapered, and flanged compression test specimens are summarized in Fig. 9.

The variety of strain combinations available in compression tests offers the possibility for material testing over most of the strain combinations that occur in actual metalworking processes. A number of samples of the same material and condition are tested, each one under different friction and geometry parameters. Tests are carried out until fracture is observed, and the local axial and circumferential strains are measured at fracture. Figures 10 to 12 give some examples of results for AISI 1045 carbon steel, 2024-T351 aluminum alloy at room temperature, and 2024-T4 alloy at a hot-working temperature. In some cases, the fracture strains fit a straight line of slope −½; in others, the data fit a dual-slope line with slope −½ over most of the range and slope −1 near the tensile strain axis. Similar data have been obtained for a wide variety of materials. In each case, the straight line behavior (single or dual slope) appears to be characteristic of all materials, but the height of the line varies with the material, its microstructure, test temperature, and strain rate.

The nature of the fracture loci shown in Fig. 10 to 12 suggests an empirical fracture criterion representing the material aspect of workability. The strain paths at potential fracture sites in material undergoing deformation processing (determined by measurement or mathematical analysis) can then be compared to the fracture strain loci. Such strains can be altered by process parameter adjustment, and they represent the process input to workability. If the process strains exceed the fracture limit lines of the material of interest, fracture is likely. Other approaches to establishing fracture criteria, as well as applications of the criteria, are given in the following two sections of this article, "Theoretical Fracture Models and Criteria" and "Applications."

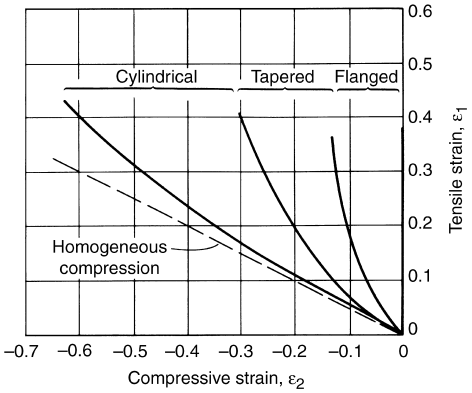

Fig. 9 Range of free surface strain combinations for compression tests having cylindrical (Fig. 2), tapered, and flanged (Fig. 8) edge profiles. The ranges shown are approximate and they may overlap a small amount.

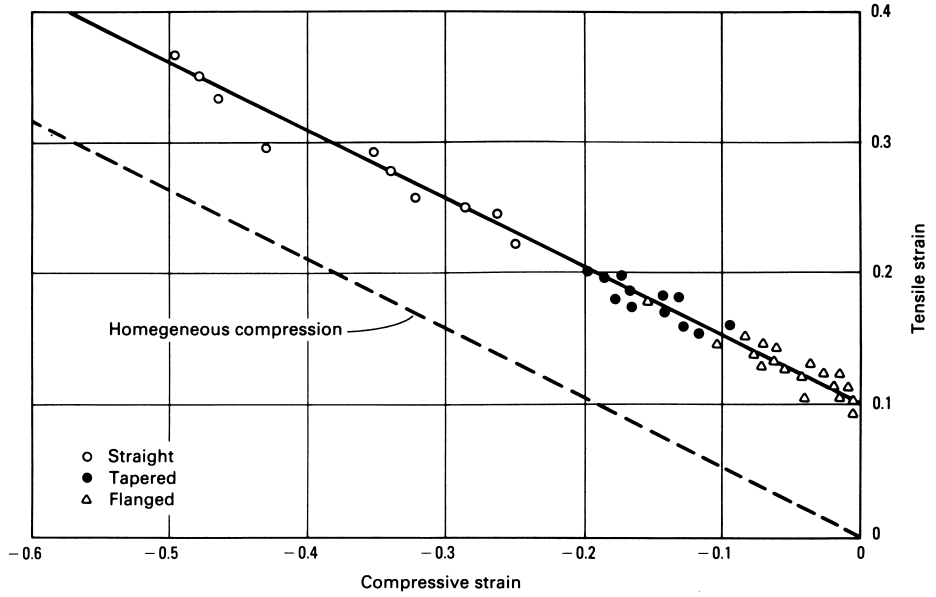

Fig. 11 Fracture locus for aluminum alloy 2024-T351 at room temperature

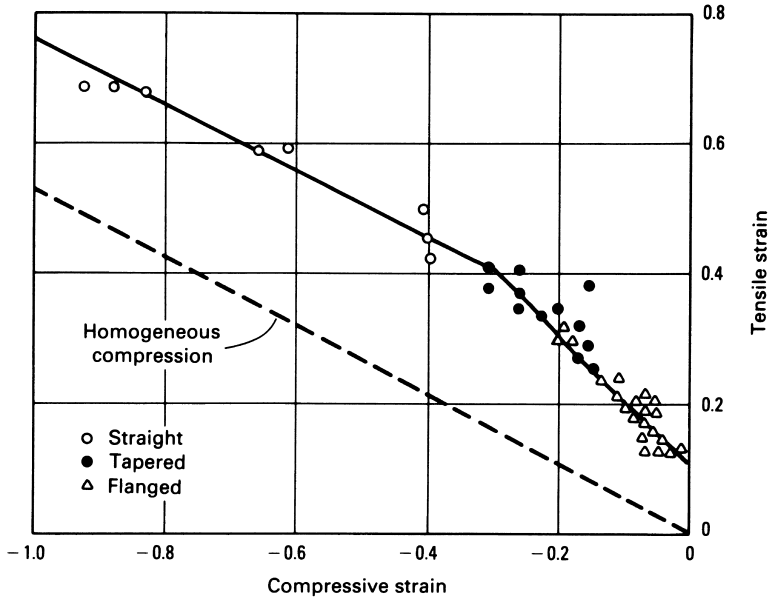

Fig. 10 Fracture locus for AISI 1045 cold-drawn steel

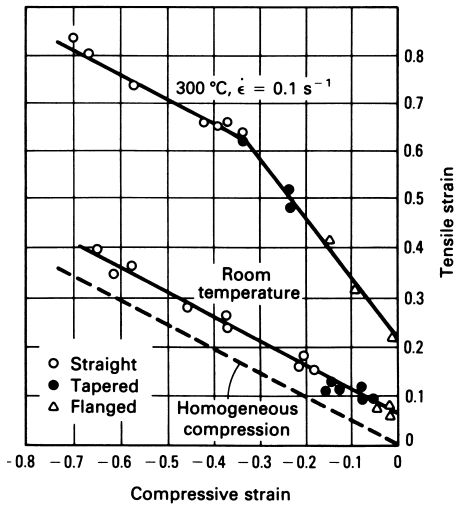

Fig. 12 Fracture locus for aluminum alloy 2024-T4 at room temperature and at 300 °C (570 °F). $\dot{\varepsilon}$ = 0.1 s^{-1}

Theoretical Fracture Models and Criteria

Fracture criteria for metalworking processes have been developed from a number of viewpoints, as described in Chapters 1 and 2. The most obvious approach involves modeling of the void coalescence phenomenon normally associated with ductile fracture. Another approach involves a model of localized thinning of sheet metal that has been adapted to bulk forming processes. In addition to models of fracture, criteria have been developed from macroscopic concepts of fracture. The Cockcroft criterion is based on the observation that both tensile stress and plastic deformation are necessary ingredients, which lead to a tensile deformation energy condition for fracture. The upper bound method has been used to predict fracture in extrusion and drawing. Other approaches are based on the calculation of tensile stress by slip-line fields.

Void Growth Model. Microscopic observations of void growth and coalescence along planes of maximum shear leading to fracture have led to the development of a model of hole growth (Ref 4). Plasticity mechanics is applied to the analysis of deformation of holes within a shear band. When the elongated holes come into contact, fracture is considered to have occurred (Fig. 13). When the McClintock model is evaluated for a range of applied stress combinations, a fracture strain line can be constructed.

Figure 14 shows the calculated results from the McClintock model in comparison with the experimental fracture line. The predicted fracture strain line has a slope of $-\frac{1}{2}$ over most of its length, matching that of the experimental fracture line. Near the tensile strain axis, the slope of the predicted line is -1, matching that of actual material results shown in Fig. 10 and 12.

Localized Thinning Model. In sheet forming, the observation that a neck forms before fracture, even under biaxial stress conditions in which localized instability cannot occur, has prompted consideration of the effects of inhomogeneities in the material. For example, a model of localized thinning due to a small inhomogeneity has been devised (Ref 5). Beginning with the model depicted in Fig. 15, plasticity mechanics is applied to determine the rate of thinning of the constricted region t_B in relation to that of the thicker surrounding material t_A. When the rate of thinning reaches a critical value, the limiting strains are considered to have been reached, and a forming limit diagram can be constructed. The analysis includes the effects of crystallographic anisotropy, work-hardening rate, and inhomogeneity size.

This model was applied to free surface fracture in bulk forming processes because of evidence that localized instability and thinning also precede this type of ductile fracture (Ref 6). Two model geometries were considered, one having a groove in the axial direction (Z-model) and the other having a groove in the radial direction (R-model) as shown in Fig. 15. Applying plasticity mechanics to each model, fracture is considered to have occurred when the thin region, t_B, reduces to zero thickness. When these fracture strains are plotted for different applied stress ratios, a fracture strain line can be constructed. As shown in Fig. 16, the predicted fracture line matches the essential features of the experimental fracture lines. The slope is $-\frac{1}{2}$ over most of the strain range and approximately -1 near the tensile strain axis. Again, this model is in general agreement with the dual-slope fracture loci shown in Fig. 10 and 12.

Cockcroft Model. The Cockcroft criterion of fracture is not based on a micromechanical model of fracture but simply recognizes the macroscopic roles of tensile stress and plastic deformation (Ref 7). It is suggested that fracture occurs when the tensile strain energy reaches a critical value:

$$\int_0^{\bar{\varepsilon}_f} \sigma^* \, d\bar{\varepsilon} = C$$

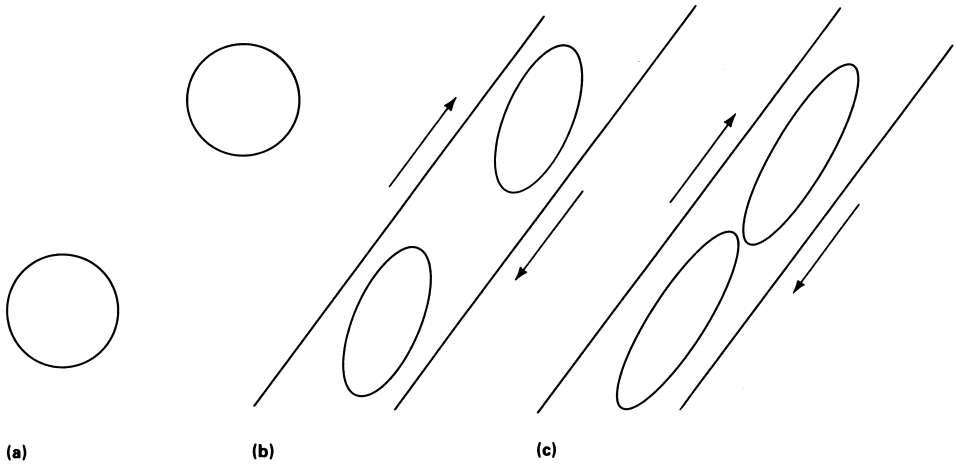

Fig. 13 McClintock model of void coalescence by shear from (a) initial circular voids, through (b) growth, and (c) void contact

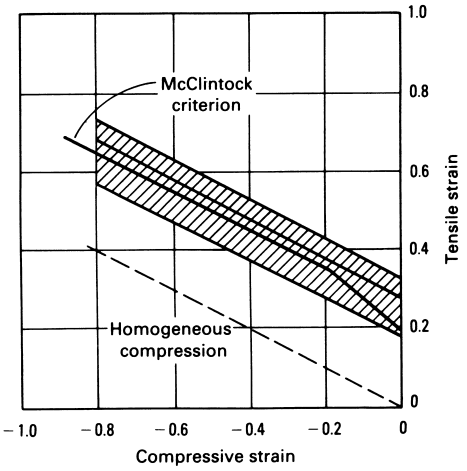

Fig. 14 Fracture strain locus predicted by the McClintock model of void growth. The shaded area represents typical experimental fracture loci such as Fig. 10 to 12.

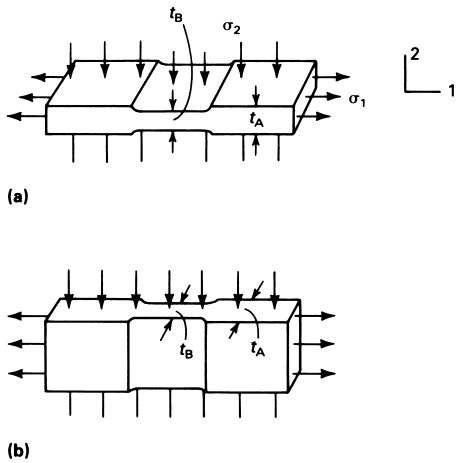

Fig. 15 Models for the analysis of localized thinning and fracture at a free surface. (a) R-model. (b) Z-model. Source: Ref 6

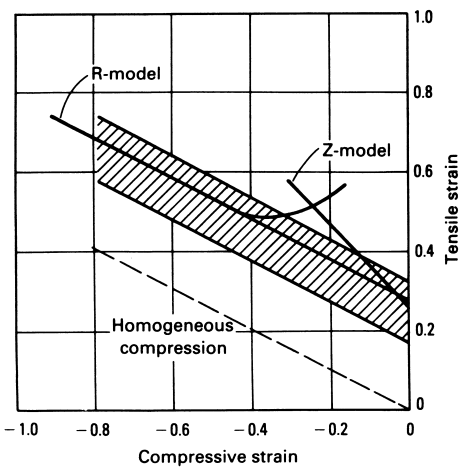

Fig. 16 Fracture strain locus predicted by the model of localized thinning. The shaded area represents typical experimental fracture loci.

where σ^* is the maximum tensile stress; $\bar{\varepsilon}$ is the equivalent strain; and C is a constant determined experimentally for a given material, temperature, and strain rate. The criterion has been successfully applied to cold-working processes. It has also been reformulated to provide a predicted fracture line for comparison with the experimental fracture strain line. Figure 17 shows that the fracture strain line predicted by the Cockcroft criterion is also in reasonable agreement with experimental results. This criterion does not show the dual-slope behavior of the previous models and some actual materials. The question of why some materials exhibit the dual-slope fracture locus and others only a single slope remains the subject of speculation, discussion, and further study.

The upper bound method of plasticity analysis requires the input of a flow field in mathematical function form. The external work required to produce this flow field is determined through extensive calculation. This value for external work is an upper bound on the actual work required. Through optimization procedures, the flow field can be found that minimizes the calculated external work done, and this flow field is closest to the actual metal flow in the process under analysis. The upper bound method has been applied to a number of metalworking processes (Ref 8).

In consideration of metal flow fields, perturbations can be incorporated that simulate defect formation. In some situations, the external work required to create the flow field with defects is less than the work required to create the flow field without defects (sound flow). According to the upper bound concept, defects would occur in these situations.

The upper bound method has been applied to the prediction of conditions for central burst formation in extrusion and wire drawing. As shown in Fig. 18, for die angles less than α_1, sound flow requires less drawing force than flow with central burst formation. Above α_2, extrusion with a dead metal zone near the die requires lower drawing force. In the range of die angles between α_1 and α_2, central burst is energetically more favorable (Ref 9).

Repeated calculations using the upper bound method provide the combinations of die angle and reduction that cause central burst (Fig. 19). Friction at the die contact surface affects the results. If operating conditions are in the central burst region, defects can be avoided by decreasing the die angle and/or increasing the reduction so that the operating conditions are in the safe zone. This example is a clear illustration of the role of process parameters (in this case, geometric conditions) in workability. An application of this method is given in the section "Applications" in this article.

It should be pointed out that the upper bound method for defect prediction gives only a necessary condition. The strain-hardening and strain rate hardening characteristics of the material have been included in the analysis (Ref 10), but the microstructural characteristics have been omitted. Therefore, when operating in the central burst range illustrated in Fig. 19, fracture can occur; whether or not it will depends on the material structure (voids, inclusions, segregation, and so on). When operating in the safe area shown in Fig. 19, central burst will not occur, regardless of the material structure.

Tensile Stress Criterion. The role of tensile stress in fracture is implicit yet overwhelmingly clear throughout the discussion of fracture and fracture criteria. The calculation of tensile stresses in localized regions, however, requires the use of advanced plasticity analysis methods such as slip-line fields or finite-element analysis. One result of slip-line field analysis that has wide application in workability studies is discussed here.

Double indentation by flat punches is a classical problem in slip-line field analysis (Fig. 20).

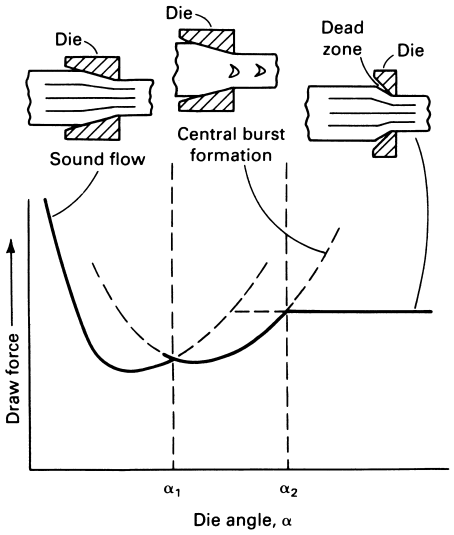

Fig. 18 Variation in mode of flow with die angle in wire drawing. The mode requiring the smallest force at any die angle is the active mode. This is a schematic for one value of reduction. Source: Ref 9

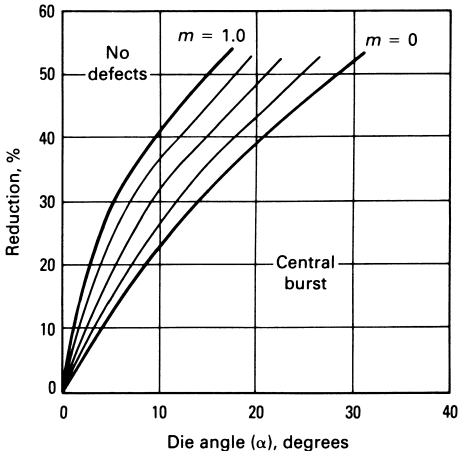

Fig. 19 Upper bound prediction of central burst in wire drawing. Increasing friction, expressed by the friction factor, m, increases the defect region of the map. Source: Ref 10

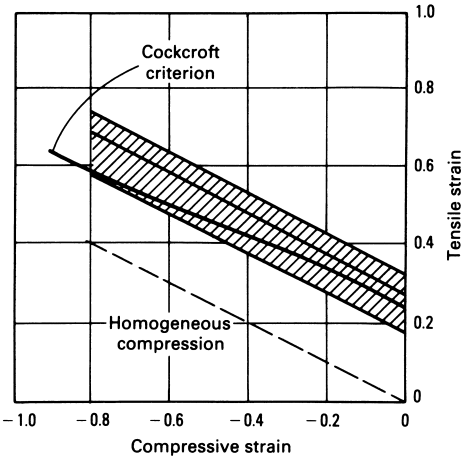

Fig. 17 Fracture strain locus predicted by the Cockcroft criterion

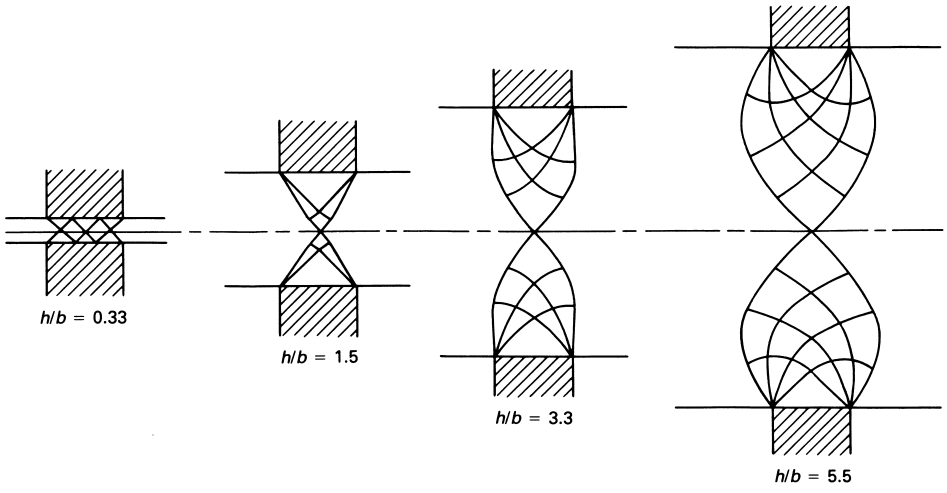

Fig. 20 Slip-line fields for double indentation at different h/b ratios. Source: Ref 11

The boundaries of the deformation zone change as the aspect ratio h/b (workpiece thickness-to-punch width) increases. For $h/b > 1$, the slip-line field meets the centerline at a point, and for $h/b < 1$, the field is spread over an area nearly as large as the punch width.

This tooling arrangement and deformation geometry approximates several other metalworking processes, as shown in Fig. 21. For similar h/b ratios in these processes then, the stresses throughout the deformation zone of the process can be approximated by those calculated from slip-line field analysis for double indentation.

Most of the work on double indentation has focused on the calculation of punch pressure and the extrapolation of these results to other processes—for example, those in Fig. 21. In a very detailed study of double indentation, remarkable agreement was found between experimental results and slip-line field results (Ref 12).

For workability studies, however, it is necessary to locate and to calculate the critical tensile stresses. It can be shown that the hydrostatic stress is always greatest algebraically at the centerline of the material and that this stress is tensile for $h/b > 1.8$. The calculated results for punch pressure and centerline hydrostatic stress are given in Fig. 22. Therefore, it is necessary to specify die and workpiece geometric parameters such that $h/b < 1.8$ in order to avoid tensile stress and potential fracture at the centerline of the processes shown in Fig. 21.

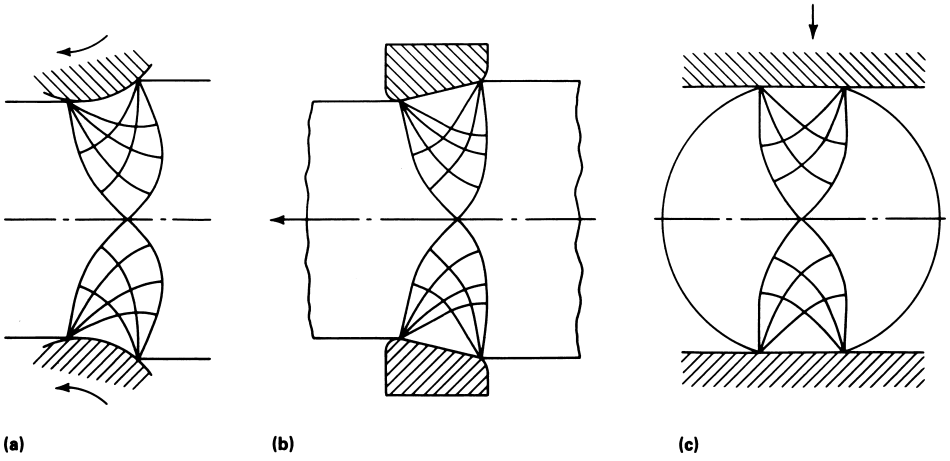

Fig. 21 Slip-line fields for (a) rolling, (b) drawing, and (c) side pressing. These fields are similar to those for double indentation shown in Fig. 20.

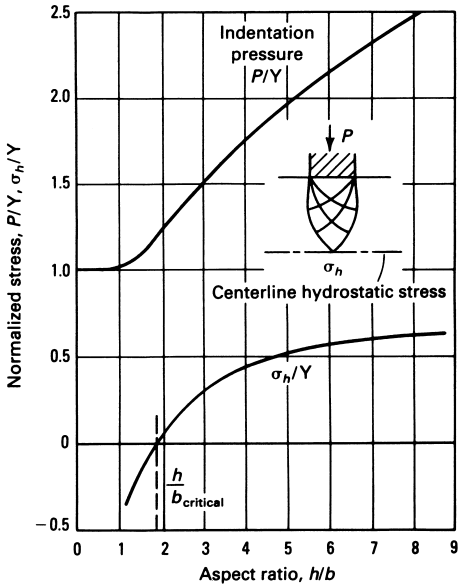

Fig. 22 Variation of the normalized indentation pressure (P/Y where Y is the yield strength) and the normalized centerline hydrostatic stress (σ_h/Y) with h/b ratio as calculated from slip-line field analysis

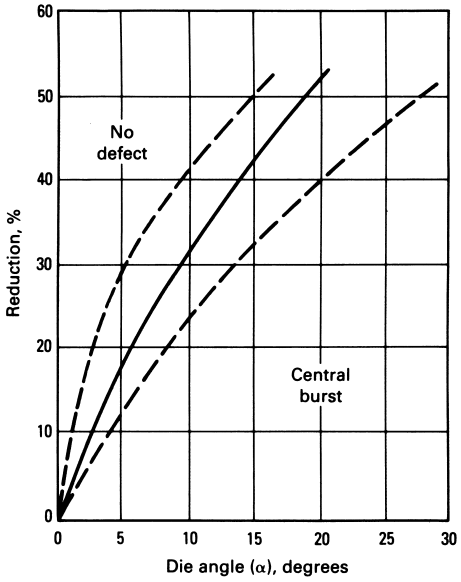

Fig. 23 Prediction of central burst in wire drawing by the tensile stress criterion and slip-line field analysis of double indentation. The range of predictions by upper bound analysis (Fig. 19) is shown by dashed lines.

For example, in extrusion, h/b is approximated by:

$$h/b = \frac{\alpha\left[1+(1-R)^{1/2}\right]^2}{R}$$

where α is the die half-angle and R is area reduction. Taking $h/b = 1.8$, the relationship between α and R that produces tensile hydrostatic stress at the centerline can be calculated. The result is given in Fig. 23, which is shown to be similar to the relationship predicted by upper bound analysis (Fig. 19). The correlation is remarkable in view of the dissimilarity in die shape between extrusion and double indentation. Furthermore, the similarity emphasizes that the flow mode for defect formation in the upper bound method is physically equivalent to the development of tensile hydrostatic stress.

As in the case of the upper bound method, the existence of a tensile hydrostatic stress does not ensure fracture, but it is a necessary ingredient. The material structure must be considered in conjunction with the tensile stress. In other words, the upper bound and tensile stress criteria are useful for defining approximate deformation limits and successful process parameters, but more detailed criteria or models are required to provide more exact values. An experimental-analytical approach in which an experimental value reflecting the inherent material ductility is determined first would be most useful (this value is used to define a point on the fracture strain locus), followed by development of the rest of the fracture-limit line, as in Fig. 10 to 12, 14, 16, and 17.

Applications

The fracture criteria discussed previously in this article can be used as tools for troubleshooting fracture problems in existing processes or for designing/modifying processes for new products. In either case, graphical representation of the criteria permits independent consideration of the process and material parameters in quantitative or qualitative form.

An example is the bolt-heading process shown in Fig. 24(a). If it is required to form a bolt head diameter D from the rod of diameter d, the required circumferential strain is $\ln(D/d)$, indicated by the horizontal dashed line in Fig. 24(b). The strain paths that reach this level, however, depend on process parameters, as shown previously in Fig. 2(b), and the fracture strain loci vary with material, as shown in Fig. 10 to 12. Referring to Fig. 24(b), if the strain path labeled a describes the strain state at the expanding free surface for one set of processing conditions and the material used has a forming limit line labeled A, then, in order to reach the required circumferential strain, the strain path must cross the fracture line, and fracture is likely to occur. As shown, one option for avoiding de-

fects is to use material B, which has a higher fracture limit. Another option is to alter the process so that strain path b is followed by the material. The latter option represents a process change, which in this case involves improved lubrication, as shown in Fig. 2. This procedure has been quantified and implemented in a computerized tool for upsetting process design (Ref 13).

In more complex cases, other means are available for altering the strain path, such as modification of die design, workpiece (preform) design, and redistribution of lubricant. Examples of application to powder forging preform design and other metalworking processes are given in Ref 14 and Ref 15.

The workability concept presented earlier in this article provides a useful supplement to the experience and intuition of the die designer, because it presents a graphical and quantitative description of the relationship between material and process parameters. Some examples of the application of the workability analysis procedures already described follow.

Bar Rolling. As shown in Fig. 3, the strains at the edges of bars during rolling are similar to those at the bulging free surface of a cylinder during compression. It should be possible, then, to predict fracture in bar rolling from compression tests on the alloy of interest. This is pertinent in current attempts to roll ingots of high alloy content into bar form. The complete workability study of bar rolling includes physical modeling of bar rolling to obtain the strain states at the edges of the bar, compression tests to obtain the material fracture limits, and comparison of the two sets of results to establish roll pass reduction limits.

Such a study is illustrated by the analysis of cracking during the rolling of 2024-T351 aluminum alloy bars. The intent was to roll square bars into round wire without resolutioning. Rolling was done on a two-high reversible bar mill with 230 mm (9 in.) diam rolls at 30 rpm (approximate strain rate: $4s^{-1}$). The roll groove geometry is shown in Fig. 25. Defects occurred primarily in the square-to-diamond passes (1–2 and 3–4), but the two diamond-to-square passes (2–3 and 4–5), the square-to-oval pass (5–6), and the oval-to-round pass (6–7) also were examined for completeness.

Lead was used as the simulation material for the physical modeling of bar rolling. Pure (99.99%) lead was cast and extruded into 25 mm (1 in.) round bars and then squared in the box pass (step 1, Fig. 25). Grids were placed on the lateral edges of the bars by an impression tool, and the grid spacing was measured before and after each pass for calculation of the longitudinal, ε_1, and vertical, ε_2, strains. Different reductions in area were achieved by feeding various bar sizes and by changing roll separation distances. A transverse slice was cut from the bars after each pass for measurement of the cross-sectional area and calculation of the reduction.

Results of the strain measurements are summarized in Fig. 26, in which tensile strain is plotted simultaneously with the compressive strain and reduction. As expected, the square-to-diamond passes involve the least compressive vertical strain, and the square-to-oval pass has the greatest compressive strain. The tensile strain versus reduction plot is the same for all cases, reflecting volume constancy.

Compression tests were performed on the 2024 aluminum alloy at room temperature and at 250 °C (480 °F) at a strain rate of $4s^{-1}$ to determine fracture limit lines. Straight, tapered, and flanged specimen profiles were used. Results are given in Fig. 27. Superposition of Fig. 26 onto Fig. 27 gives the rolling deformation limits.

To test the workability predictions, aluminum alloy bars were rolled at room temperature and at 250 °C (480 °F). Grid and area reduction measurements were made for the square-to-diamond passes. Figure 28 shows the measured strains at room temperature, which agree with

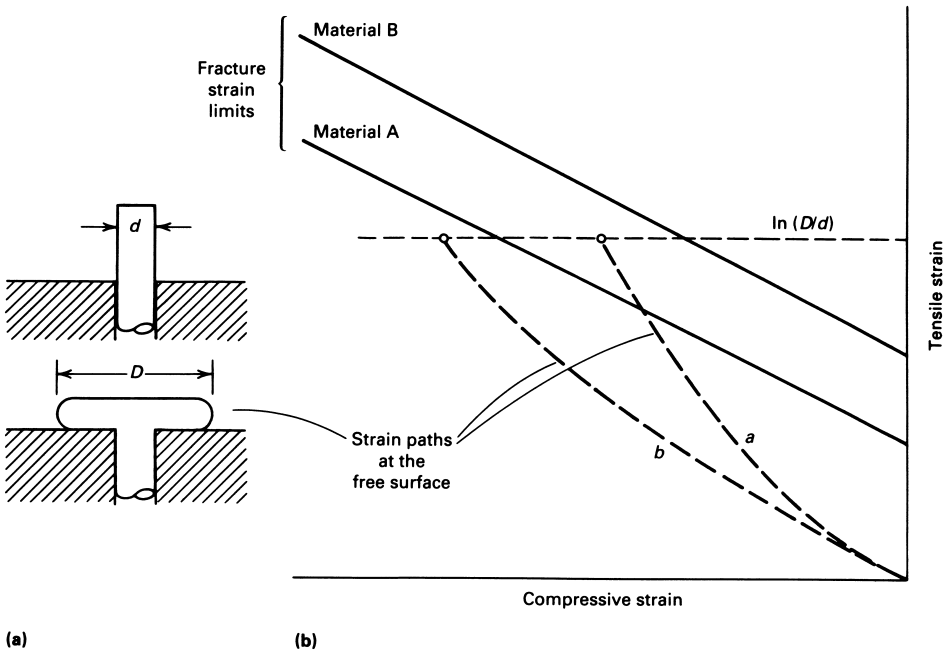

Fig. 24 Upsetting (a) of bar diameter *d* to head diameter *D*. (b) Material fracture strain limits are superimposed on strain paths reaching the final required strain. Strain path b (low friction) prevents fracture for both materials. Material B avoids fracture for either strain path.

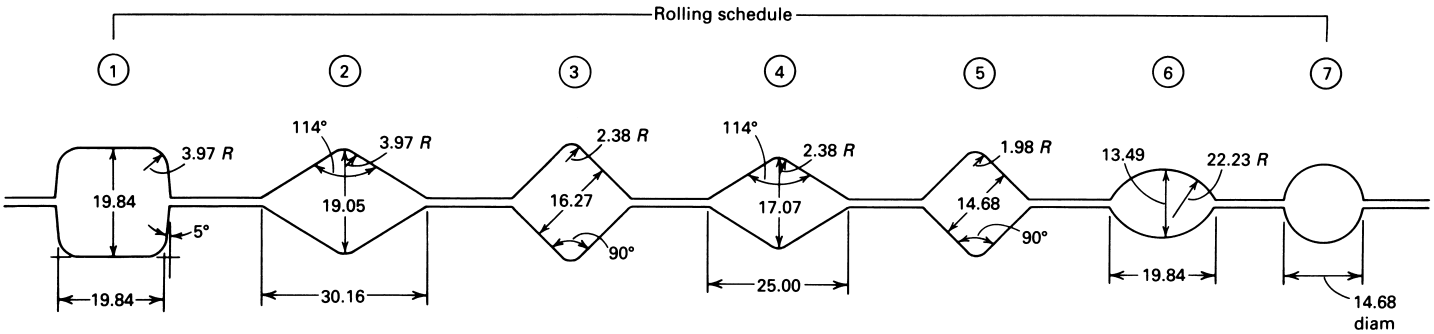

Fig. 25 Roll groove geometry for rolling square bars into round wire. Dimensions given in millimeters

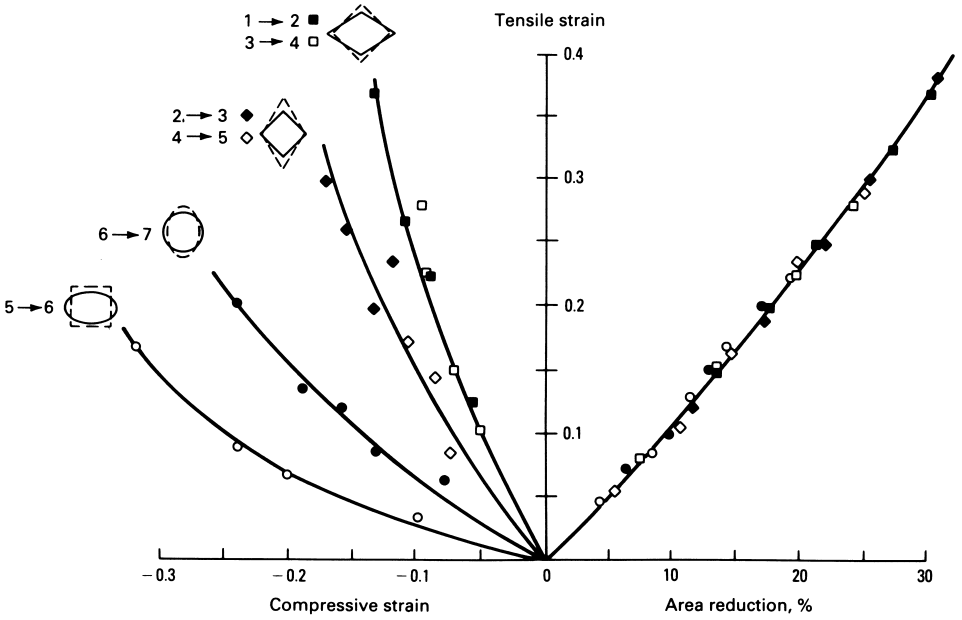

Fig. 26 Measured localized strains during the rolling of lead bars. Left side shows longitudinal tensile strain versus vertical compressive strain. Right side shows longitudinal strain versus cross-sectional area reduction at room temperature.

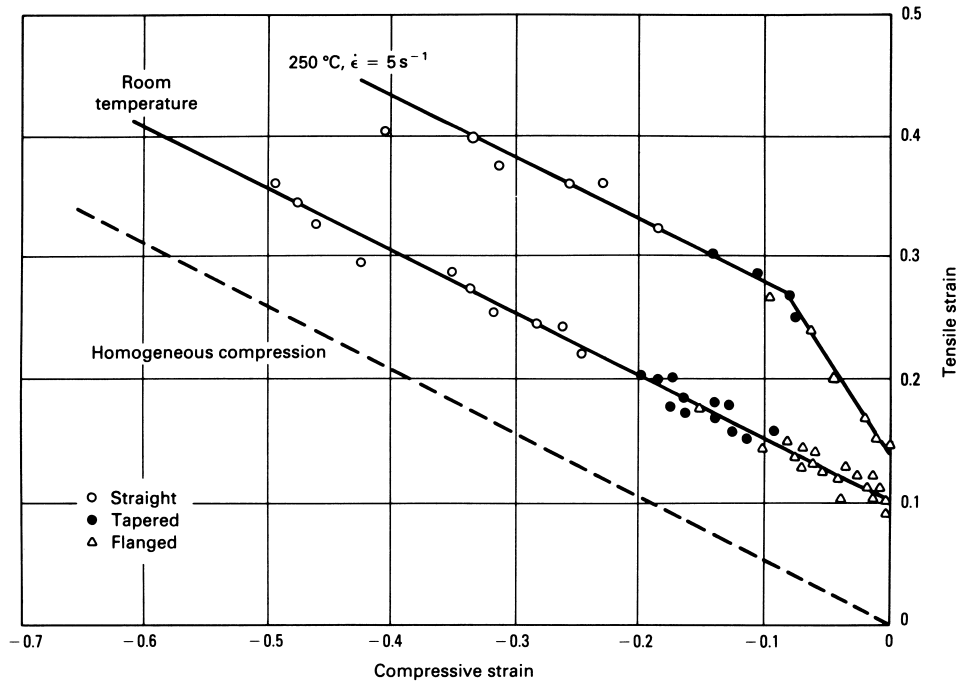

Fig. 27 Fracture strain lines for 2024 aluminum alloy in the T351 temper, measured by compression tests at room temperature and at 250 °C (480 °F)

those measured in lead bars for the same pass (Fig. 26). Open circles indicate fracture, and closed circles indicate no fracture. The fracture line for the aluminum alloy at room temperature is superimposed as the dashed line. It is clear that edge cracking in bar rolling conformed with the material fracture line, and the limiting reduction is approximately 13% for this combination of material and pass geometry. Similarly, at 250 °C (480 °F), there was conformance between fracture in bar rolling (Fig. 29) and the fracture line of the alloy (Fig. 28). In this case, the limiting reduction is approximately 25%.

Extrapolating the preceding results for cold rolling, the limiting reduction for diamond-to-square passes would be approximately 15%; for the oval-to-round pass, approximately 20%; and for the square-to-oval pass, approximately 25%. Similarly, in the hot rolling of this aluminum alloy, the reduction limit for diamond-to-square passes would be approximately 27%; for oval-to-round passes, approximately 30%; and for square-to-oval passes, approximately 40%. The latter two are beyond the reduction normally used because of fin formation, so cracking occurs rarely in such passes.

Example 1: Preform Design for a Ball Bearing Race. A low-load high-torque ball bearing outer race was cold forged from a low-alloy steel powder preform (Fig. 30). The preforms were compacted from 4600 grade powder with carbon added to give 0.20% C in the sintered material. The sintered preforms were 80% of theoretical density.

Initial efforts led to cracking through the preform along a diagonal beginning at the point of contact between the punch and preform (Fig. 31). The large shear stress developed by the contact was beyond the fracture limit of the porous preform, and two solutions were considered that would avoid such stresses (Fig. 32). The first solution was the use of a flat preform that involves back extrusion flow into the outer rim, and the second was the use of a tall, thin-wall preform that involves radial inward flow into the inner flange. The first option was rejected because it would generate circumferential tension that would most likely cause fracture. The second option is desirable because compression is applied at the top face; this option was pursued through physical modeling.

The primary concern with the second option (Fig. 32b) was the large amount of radially inward deformation required to form the inner flange. As a result, this option was examined by physical modeling. Model preforms were produced from sintered 601AB aluminum alloy powder and gridded on the inside surface (Fig. 33a). Grid displacements were measured after each of several increments of deformation, and the calculated strains were plotted along with the fracture line of the material (Fig. 33b). It is clear that both the axial and circumferential strains are compressive throughout the process and do not exceed the fracture line. Some wrinkling of the inside surface occurred, but this was smoothed out when the surface contacted the mandrel under pressure.

Actual production of straight-wall preforms as in Fig. 33(a) was not feasible, because the height-to-thickness ratio is too large for compaction. A compromise was developed in which the preform angle was 17° instead of 30°, as used in the original preform, or 0°, as used in the physical model (Fig. 33b). This ensured initial punch contact at the top face of the preform and generated compressive strains on the inside surface, as in Fig. 33(b). Cold-forging trials on these preforms produced no cracks, developed the desired full density in the ball path region, and showed the added benefit of a smooth ball path surface that did not require grinding.

Example 2: Back Extrusion of Copper Alloy. A low-ductility dispersion-strengthened copper alloy was back extruded into a cup shape,

as shown in Fig. 34. The deformation was carried out at room temperature on a mechanical press. Crack formation on the rim caused high rejection rates. The original slugs for this process were smaller in diameter (16 mm, or 0.625 in.) than the die inside diameter (19 mm, or 0.75 in.), as shown in Fig. 35(a). Deformation of such preforms involves circumferential expansion strain (equal to ln (D/d), where D is the die bore diameter and d is the slug diameter) along with very little compressive strain at the rim (Fig. 35b). For this case, the circumferential strain is ln (0.75/0.625) = 0.18. Workability analysis would then require only measurement of the material fracture line and comparison with the required circumferential strain 0.18.

Fracture strains were measured in flange compression tests as shown in Fig. 36, giving a minimum circumferential strain of 0.2, which is sufficiently above the required strain for avoidance of fracture. A hydraulic press was used (giving a strain rate of approximately 0.5 s^{-1}), on the assumption that there is no strain rate effect at room temperature. Because the workability analysis showed that fracture should not be a

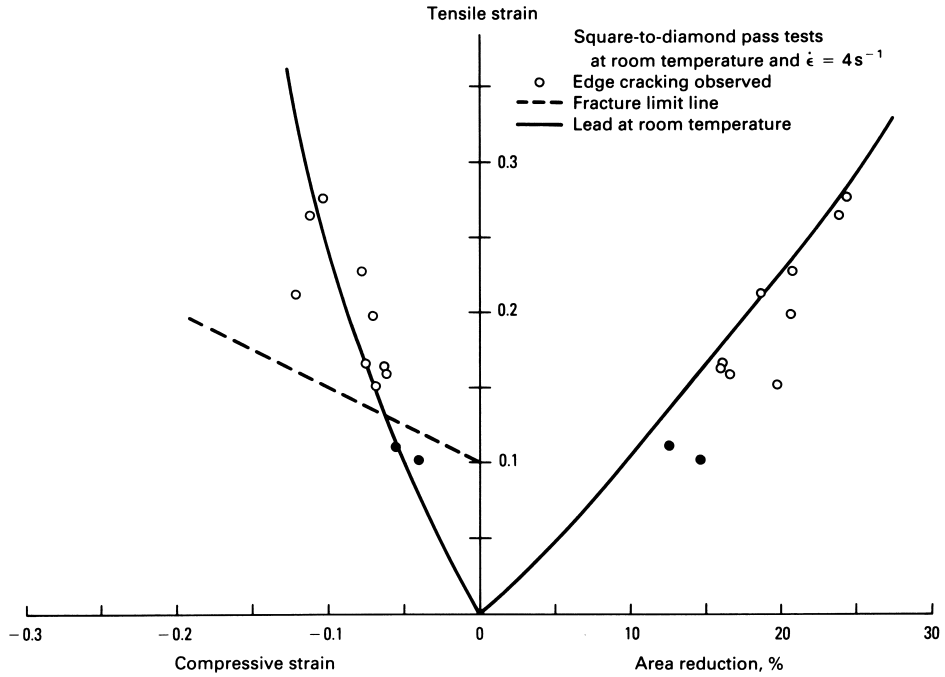

Fig. 28 Superposition of fracture line (dashed) on measured strains during rolling of 2024-T351 aluminum alloy bars at room temperature. Solid line represents the strain path measured during rolling of the lead model material shown in Fig. 26.

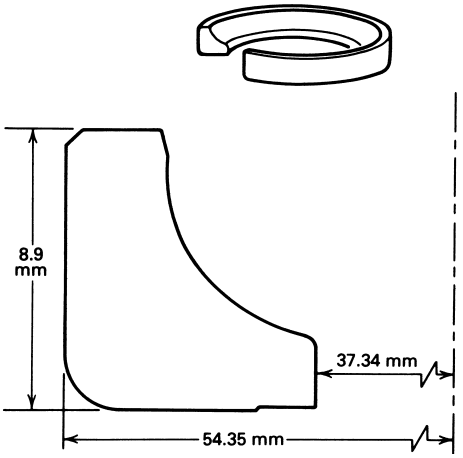

Fig. 30 Ball bearing outer race that was cold forged from sintered powder preform of 4620 low-alloy steel

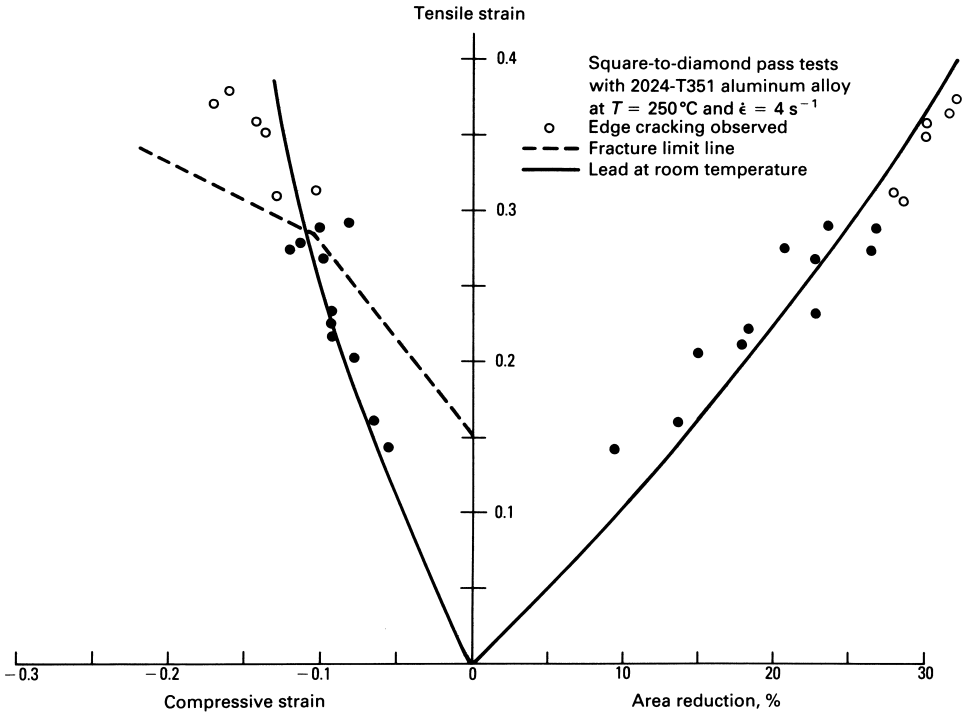

Fig. 29 Superposition of fracture line (dashed) on measured strains during the rolling of 2024-T351 aluminum alloy bars at 250 °C (480 °F). Solid line represents the strain path measured during rolling of the lead model material shown in Fig. 26.

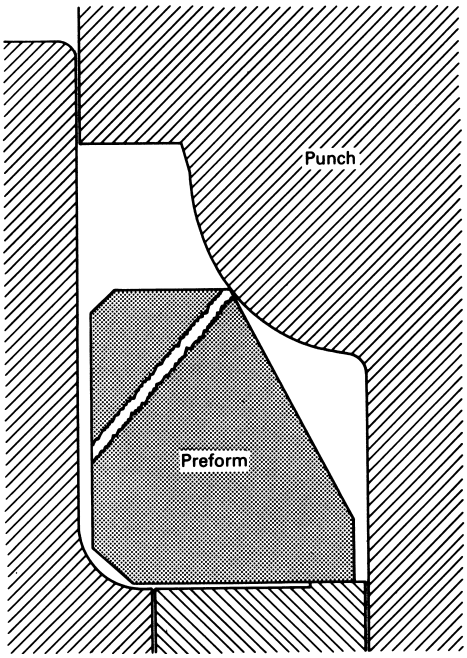

Fig. 31 Cracks initiated at the point of contact between the punch and preform in the original preform design. The preform had a taper of 30° on the inside diameter.

problem, the effect of strain rate was explored further.

Tests were performed on the same alloy using controlled strain rate servohydraulic test equipment at strain rates of 5, 10, and 15 s^{-1}; the third strain rate given is close to that in the production mechanical press. Figure 37 shows the surprising result that the fracture limit line decreases with increasing strain rate. In particular, the minimum circumferential strain falls below the required value of 0.18 for successful forming of the rim; this explains the occurrence of fracture on the production press. The problem was corrected by using slugs of larger diameter to decrease the circumferential tension and by preforming a taper on the top face (Fig. 38), which produced some axial compression in the material at the rim. The strain path then avoided crossing the fracture line (Fig. 39), and the rejection rate during production on the mechanical press was nil.

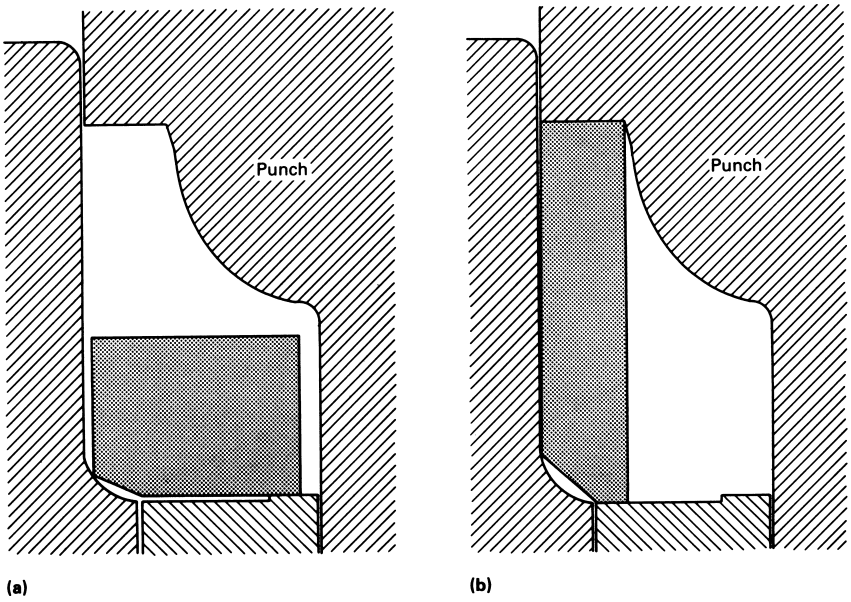

Fig. 32 Preform alternatives for forging the ball bearing outer race shown in Fig. 30. (a) Back extrusion. (b) Compression and radial inward flow

Contact Surface Fracture and Internal Fracture. All of the previous applications and examples involved free surface fractures and could be treated directly by the fracture line. Consideration of contact surface fractures (Fig. 5) and internal fracture (Fig. 6), however, requires modification of this approach or use of a new approach. In the following, an example is given of the application of the upper bound and tensile stress criteria to central burst in extrusion. The empirical workability concept described previously is then modified for application to contact surface fracture as well as central burst.

Example 3: Central Burst During Extrusion. Central burst can occur in extrusion when light reductions and large die angles are used (Fig. 19), and it is encountered in the production of shafts for transmissions and suspension systems. A test of the central burst criterion was carried out by processing shafts from hot-rolled 1024 steel bars 22 mm (⅞ in.) in diameter (Ref 16). The processing sequence consisted of initial drawing followed by three extrusion steps in a boltmaker:

Process	Reduction, %	Die half-angle, degrees
Drawing	8	9
Extrusion	22	22.5
Extrusion	23	22.5
Extrusion	16	22.5 or 5

All passes are in the central burst area of Fig. 40, except for the last pass with a 5° die angle.

A total of 1000 shafts were processed with the 22.5° die, and 500 shafts were processed with the 5° die. All shafts were tested ultrasonically for internal defects. Central bursting was de-

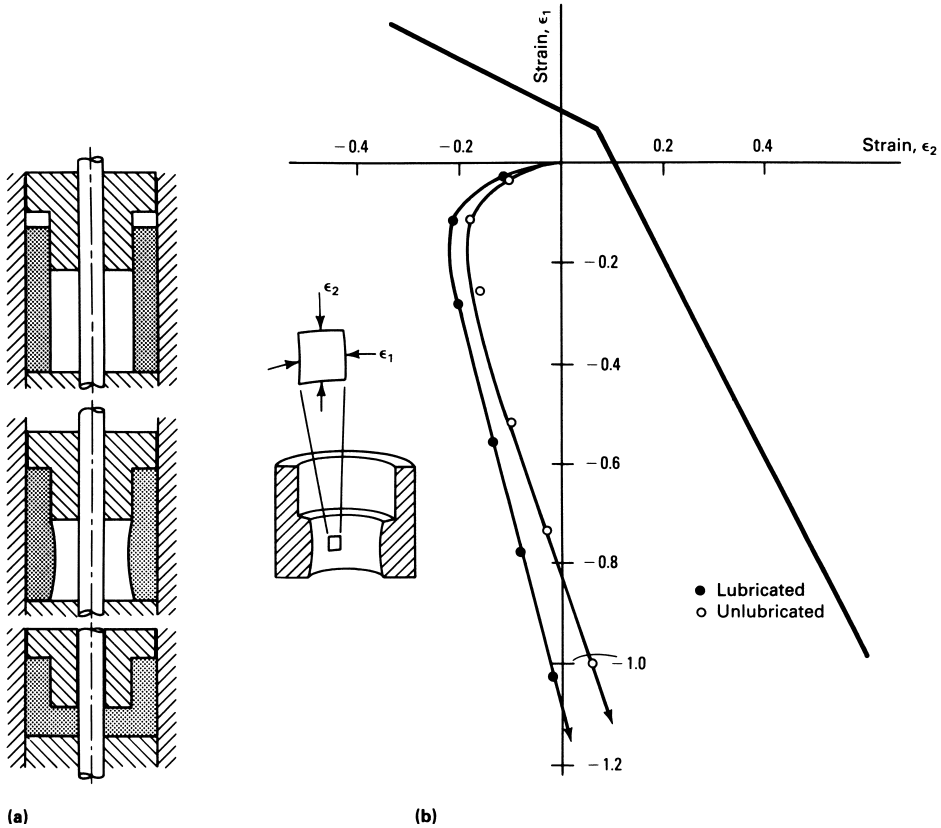

Fig. 33 (a) Physical model for the second option (Fig. 32b) and (b) the measured strains during forging of the preform. The heavy line is the material fracture line. It is clear that the strain path never crosses the fracture line and that defects are prevented.

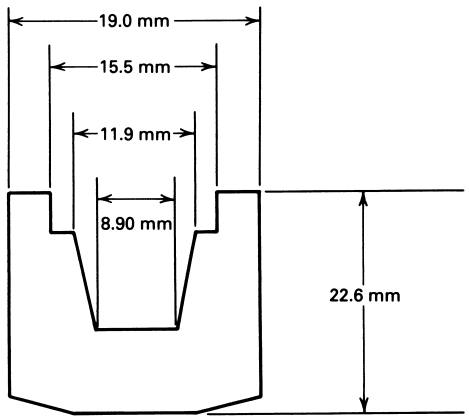

Fig. 34 Part that was back extruded from copper

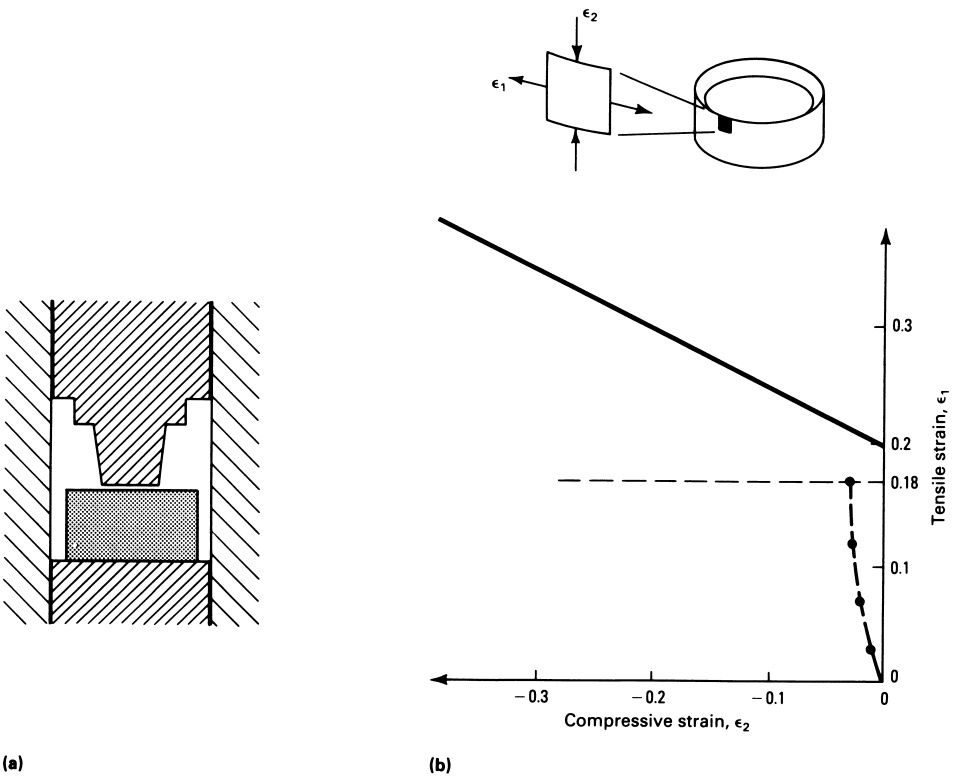

Fig. 35 Back extrusion of the cup shape shown in Fig. 34. (a) The preform slug was 16 mm (0.625 in.) in diameter, the die was 19 mm (0.75 in.) in diameter. (b) Strains at the cup rim where fracture occurred consist of circumferential tension to a value of 0.18 and very little compressive strain. The heavy line is the material fracture strain line.

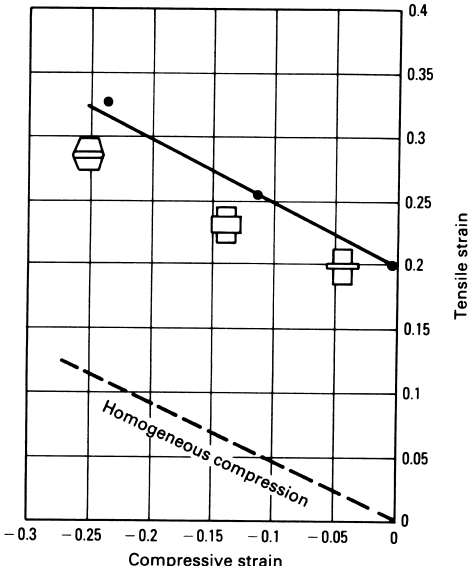

Fig. 36 Fracture strain line for copper alloy, determined by flanged and tapered compression tests. Specimen geometries used for each test are shown also.

tected in 4.5% of the shafts extruded with the 22.5° die, and no defects were detected in the shafts extruded with the 5° die. These results show that the upper bound central burst criterion is a necessary condition. It was further shown in Ref 16 that central burst was avoided in other heats with slightly different compositions because their strain-hardening coefficients were larger than the original heat. This confirmed the predicted results in Ref 10.

Modified Empirical Criterion. It was shown previously in this article that measured free surface strains at fracture fit a linear or bilinear line that constitutes a fracture locus for the material tested (Fig. 10 to 12). This is a convenient representation of the complexities of ductile fracture that are controlled by stress and deformation. The experimental fracture locus is also reproduced by several theoretical fracture criteria (Fig. 14, 16, and 17).

For contact surface and internal fractures, however, the surface on which the strains can be monitored is subjected to stress normal to that surface. It was shown in Eq 3 that stress states leading to a given set of surface strains differ only by a hydrostatic stress component, and this component is equal to the applied stress normal to the surface on which the strains are monitored. Experience shows that this hydrostatic stress affects fracture, and it should also affect the fracture strain locus. It should be possible, then, to use the theoretical fracture criteria to predict the effects of hydrostatic stress on the fracture strain locus.

The simplest criterion described previously in this article is that due to Cockcroft; therefore, it was modified to predict the effects of stress normal to the plane (Fig. 5 and 6) on the fracture strains ε_1 and ε_2. The result (Fig. 41) shows that superimposed pressure ($P > 0$) increases the

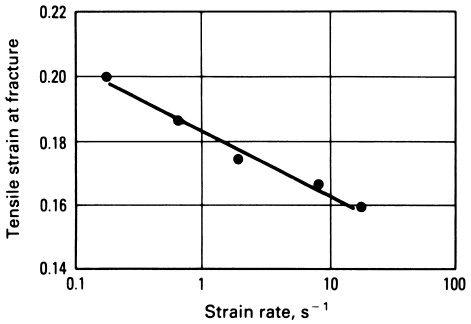

Fig. 37 Decrease in circumferential tensile strain at fracture with increasing strain rate for the copper alloy tested in Fig. 36. Results are for thin-flanged compression specimens, which have the lowest fracture strain.

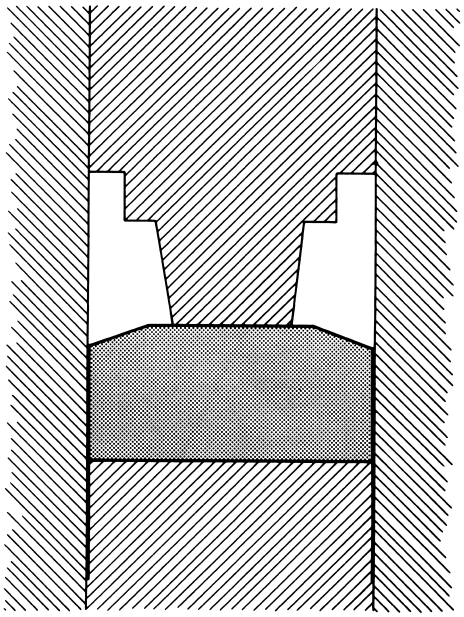

Fig. 38 Modified preform slug for the back extrusion of the cup shape shown in Fig. 34. The slug diameter is 18.8 mm (0.74 in.) and has a 5° taper on the top surface.

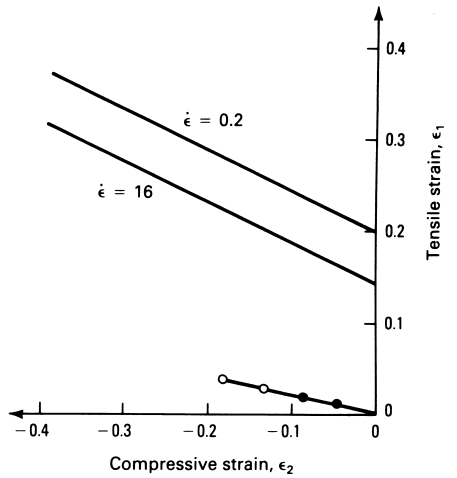

Fig. 39 Comparison of measured strains at the cup rim during back extrusion of the modified preform slug shown in Fig. 38. The strains do not exceed the material fracture strain line for low or high strain rate forming.

height of the fracture strain line and also increases its slope slightly. Superimposed tension ($P < 0$) decreases the height of the fracture line, decreases its average slope, and gives it a slight downward curvature. It is clear that the increase in strains to fracture due to additional pressure is unlimited as pressure increases, but the strains to fracture due to additional tension are limited by zero as tension increases. This result is discussed with regard to internal fracture and die contact surface fracture in the following paragraphs.

Central Burst in Forgings. Internal fractures along the centerline of extruded or drawn bars were discussed earlier (Fig. 18, 19, 23, and 40). Similar fractures are observed in forged shapes such as that shown in Fig. 42 for heat-treated 6061 aluminum alloy. Here, as the outer region is compressed between dies, material flows radially inward and then vertically into the opposed hubs. This develops a hydrostatic tensile stress state at the center (Fig. 6a), and fracture is a strong possibility.

Through visioplasticity analysis on split, gridded specimens (Fig. 42), the strain and stresses at the center of the workpiece were calculated for several increments of deformation. The hydrostatic stress state at the center of the specimen is not always tensile; initially, it is compressive, and then it reverses, becoming tensile as the flange thickness is reduced and flow into the hub occurs. Meanwhile, the strains at the center are increasing monotonically as deformation progresses. This is illustrated in Fig. 43 by the steps 0-1-2-3. As deformation proceeds, the strains at the center increase, but the hydrostatic pressure is also increasing, so the fracture line moves upward. Then, as the flange thickness approaches one-half of the hub base diameter (die orifice diameter), the hydrostatic stress becomes tensile, so the fracture line decreases in height. The strains at the center continue to rise, however, and cross the fracture line, leading to the central burst. The calculated hydrostatic tension at fracture was $0.3Y$. This approach could be used for predicting central burst in drawing and extrusion to provide a material-dependent criterion, as opposed to the more simplistic upper bound and tensile stress criteria described previously.

Die Contact Surface Fracture. Frequently, cracks occur during forging on surfaces that are in contact with the dies (Fig. 5). One common location of such defects is the vicinity of a die or punch corner. From the observation of a variety of such defects, it appears that a common characteristic is an abrupt change in frictional shear traction distribution in the region of the crack. High friction to retard metal flow in advance of the crack location is one method for preventing such defects.

A technique for studying die contact surface cracks was developed by means of a disk compression test and dies having a rough surface in the central region and a smooth surface in the outer region. Figure 44 shows the top view of a 6061 aluminum alloy disk compressed between such dies. In the transition region between the rough central die surface and the smooth outer region, radial cracks initiate and propagate outward. Such cracks occurred at approximately 30% reduction when the smooth outer region was lubricated with Teflon. The cracks occurred at approximately 45% reduction when grease lubrication was used in the outer smooth region. No cracks occurred even for very large reductions when the smooth outer region was not lubricated.

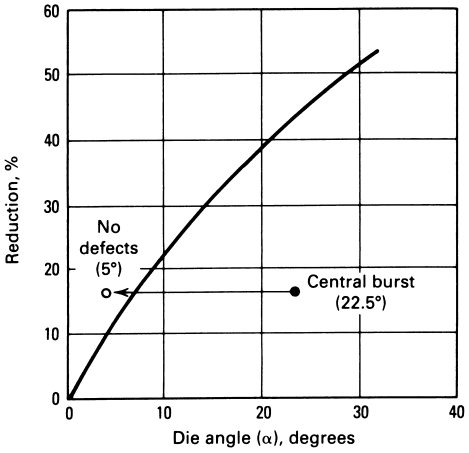

Fig. 40 Location of process conditions on a theoretical central burst map. For an angle of 22.5°, central burst occurred in 4.5% of the extruded shafts. For a die angle of 5°, no central burst occurred.

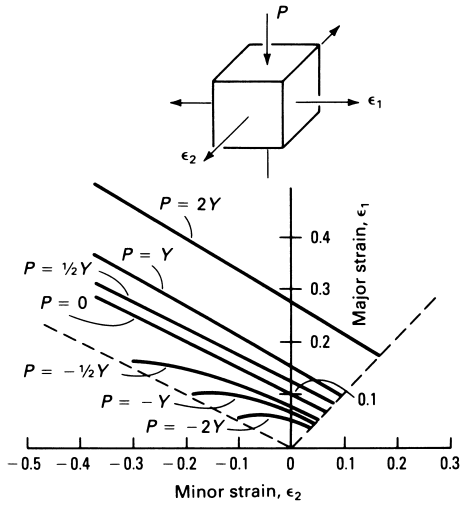

Fig. 41 Movement of the fracture strain line due to superimposed hydrostatic stress. Applied stress is represented in terms of multiples of the yield strength, Y. Negative values of P indicate hydrostatic tension. Calculations are based on a modification of the Cockcroft criterion.

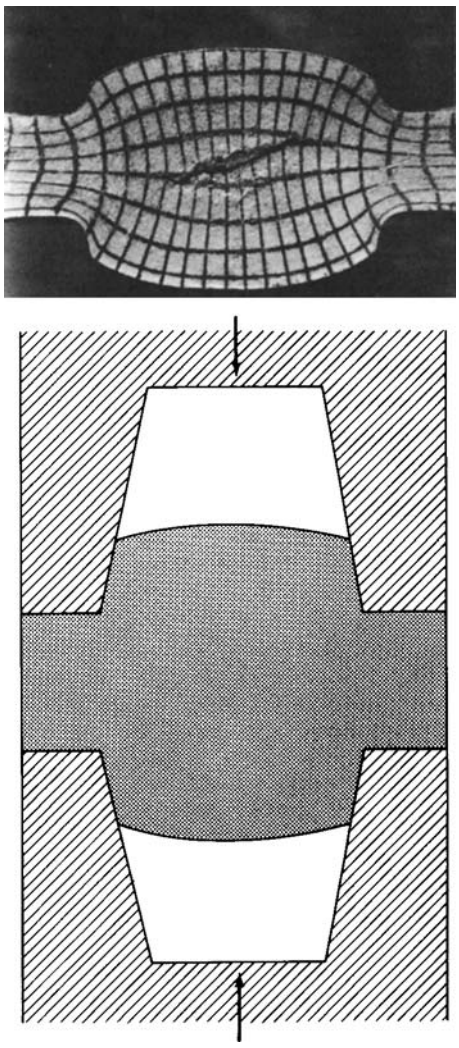

Fig. 42 Internal fracture during the double-extrusion forging of aluminum alloy 6061. Grid deformations on the middle longitudinal plane are shown. Stress and strain states are defined by Fig. 6(a).

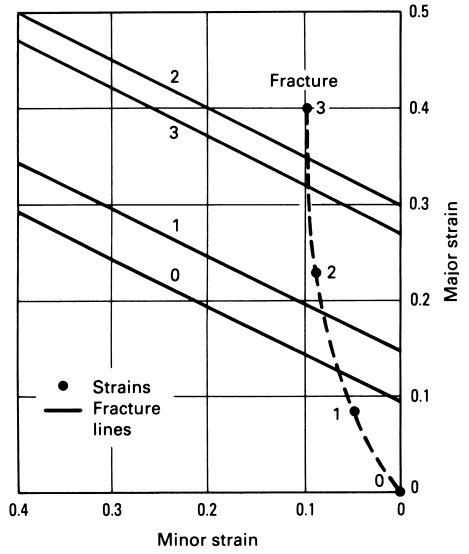

Fig. 43 Progression of surface strains and fracture line at the central internal location of the double-extrusion forging shown in Fig. 42. The fracture line rises from 0 to 1 to 2 as internal pressure increases and then falls to point 3 as the internal stress becomes tensile.

Grid marks placed on the die contact surface of the disks were used to measure the distribution of surface strains in the radial direction. Figure 45 gives an example of such measurements. In the rough central region the strains are zero, while in the smooth outer region the strains are equal and constant. In the transition, however, the circumferential strain, ε_θ, jumps abruptly from zero to its constant value in the outer region, and the radial strain, ε_r, overshoots to a very high value before returning to its constant value in the smooth outer region.

The strains shown in Fig. 45 were the same regardless of the friction condition in the smooth outer region. Therefore, fractures in the transition region occur because of the combination of large tensile surface strains and low hydrostatic stress state. This explains the occurrence of cracks at low reduction when Teflon is used, and no occurrence of fracture when no lubricant is used. The Teflon, having a near-zero friction coefficient, results in very low radial back pressure on the transition region, while grease and no lubricant provide progressively larger back pressures.

By means of visioplasticity analysis, the stresses were determined at the contact surface in the vicinity of the transition region. The resulting normal die pressure plus the surface radial and circumferential strains define the stress and strain states in the transition region and can be illustrated on a forming limit diagram. Figure 46 shows the change in surface strains and the increase in the fracture line due to increasing normal pressure during compression of a disk with grease lubricant in the outer region (indicated by the increments of reduction to 45%). The fracture line increases at a slower rate than the strains increase with increasing pressure, and at 45% reduction the strain path exceeds the fracture line and cracks are observed. For Teflon lubricant, the crossover occurs at about 30% reduction, while in the case of no lubricant the fracture line moves progressively away from the strain path.

Example 4: Fir Tree Defect. The criterion for contact surface fracture can be applied qualitatively for interpretation of the fir tree defect in extrusion. Such defects occur on the surfaces of extruded bars as well as in localized areas of forgings containing ribs. In a section of a rib-web forging from a preform of sintered aluminum alloy powder, small cracks formed with a regular spacing on the rib surfaces (Fig. 47). Such defects occurred only when the thickness of the rib was greater than approximately one-half the web length; that is, extrusion reduction was less than one-half. Each crack formed by shear at the corner as material flowed from the web into the vertical rib.

The stress and strain state on a surface material element is shown in Fig. 48. As material in the web is compressed, the surface element experiences tensile strain in the direction of flow, and the strain increases as the element approaches the die corner. At the same time, there is a compressive stress from the die onto the surface element. This pressure diminishes, however, as the element nears the die corner and almost disappears as the element moves around the corner.

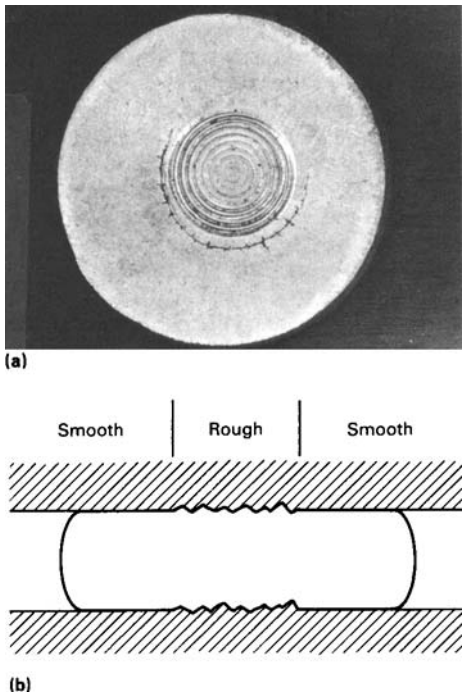

Fig. 44 (a) Top view of aluminum alloy 6061 disk compressed between dies. (b) Cracks form at the transition region between rough and smooth areas of the die.

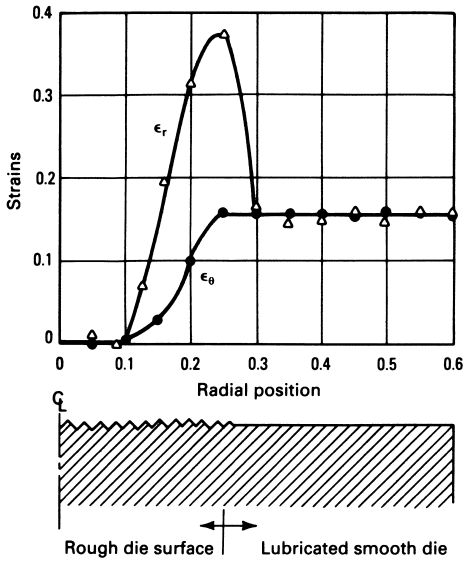

Fig. 45 Radial variation of contact surface strains after 30% compression of the disk shown in Fig. 44

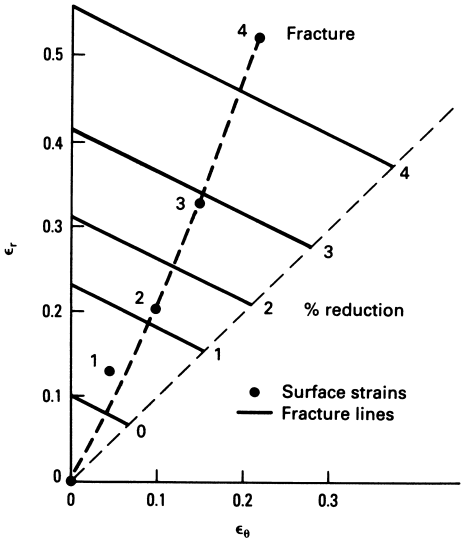

Fig. 46 Progression of surface strains and fracture line at the transition region between rough and smooth zones of the compressed disk shown in Fig. 45. Points 1, 2, 3, and 4 represent 10, 20, 30, and 45% reduction, respectively.

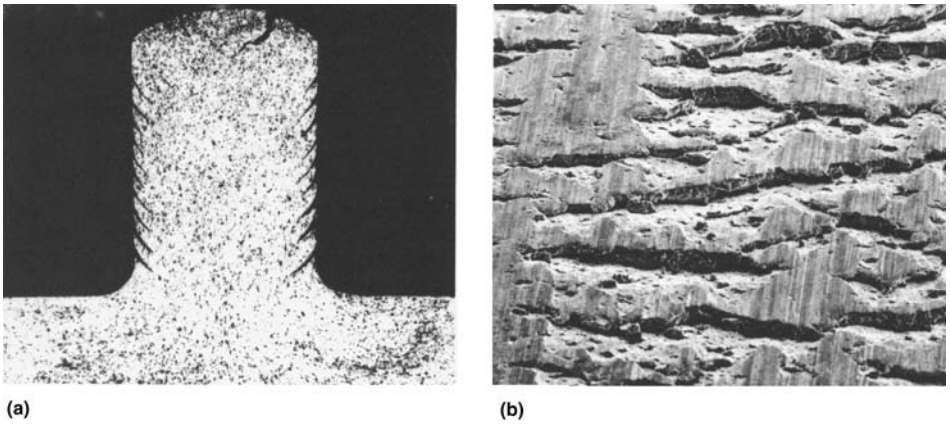

Fig. 47 Die contact surface cracking during forging extrusion of aluminum alloy powder compact. (a) Cross section. (b) Normal to vertical rib surface. Note also the cracks at the top free surface. Stress and strain states are defined in Fig. 4(b).

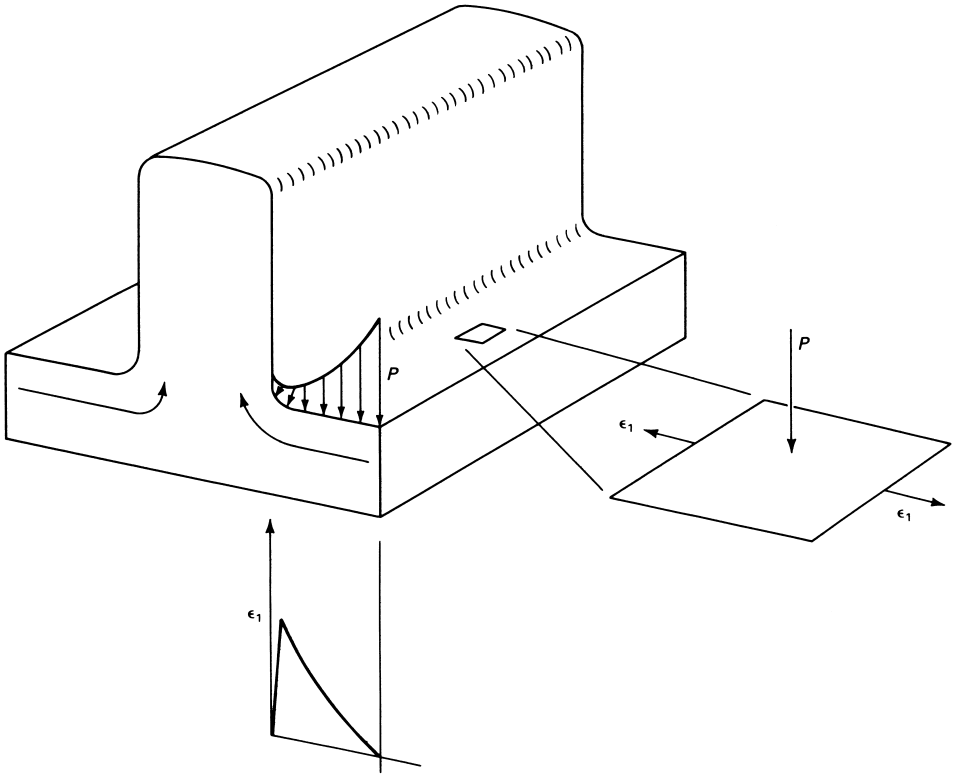

Fig. 48 Increase in strain ϵ_1, and decrease in die contact pressure P on a surface element as it moves from the web into the rib section of the extrusion forging shown in Fig. 47.

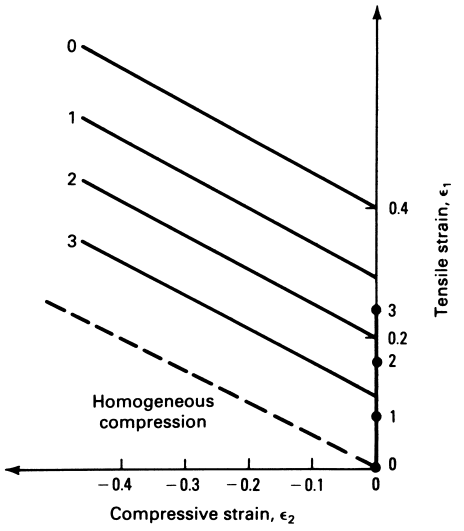

Fig. 49 Progression of strain ϵ_1, and decline of fracture line due to decrease in pressure P for an element moving from the web to rib section during the forging extrusion shown in Fig. 48. At stage 3, the strain exceeds the fracture line.

This can be illustrated schematically on the fracture strain diagram shown in Fig. 49. Because the deformation is in a state of plane strain, the strain path is represented as a vector of increasing length along the vertical axis. Meanwhile, the fracture line decreases in height because the pressure acting normal to the element is progressively decreasing. When the strains cross the fracture line, fracture occurs.

This phenomenon does not take place when extruding ribs of small thickness, because the extrusion reduction, and therefore the pressure, is larger, which maintains the fracture line at a high level. For thick ribs, two solutions were considered. One approach is to increase friction along the rib walls by roughening the die surface or avoiding lubrication of the die rib. This produces greater back pressure at the die corner, elevating the fracture line and preventing cracking. Such an approach is difficult to implement and can be used only with segmented dies because the formed rib cannot be removed from the die. The second approach is to use a draft angle on the rib, which has the same effect as increased friction. An angle of 10° prevented fracture in the current case, but other alloys may require a smaller or larger angle. A quantitative analysis combining the pressure effect on the fracture line and plasticity analysis would provide a method of predicting the draft angle in order to prevent fracture.

REFERENCES

1. H.A. Kuhn, P.W. Lee, and T. Erturk, A Fracture Criterion for Cold Forging, *J. Eng. Mater. Technol. (Trans. ASME),* Vol 95, 1973, p 213–218
2. H. Ortiz and H.A. Kuhn, Physical Modeling of Bar Rolling for Workability Study, *Physical Modeling of Bulk Metalworking Processes, Conf. Proc.,* ASM International, 1987
3. E. Erman and H.A. Kuhn, Novel Test Specimens for Workability Measurements, *Compression Testing of Homogeneous Materials and Composites,* STP 808, ASTM International, 1983, p 279–290
4. F.A. McClintock, *J. Appl. Mech. (Trans. ASME),* Vol 90, 1968, p 363
5. Z. Marciniak and K. Kuczynski, A Model of Localized Thinning in Sheet Metalforming, *Int. J. Mech. Sci.,* Vol 9, 1967, p 609
6. P.W. Lee and H.A. Kuhn, Fracture in Cold Upset Forging—A Criterion and Model, *Metall. Trans. A,* Vol 4, 1973, p 969–974
7. M.G. Cockcroft and D.J. Latham, Ductility and the Workability of Metals, *J. Inst. Met.,* Vol 96, 1968, p 33–39
8. B. Avitzur, *Metal Forming—Processes and Analysis,* McGraw-Hill, 1968
9. W.M. Evans and B. Avitzur, "Die Design for Drawing Extrusion," Paper MF67–582, Society of Manufacturing Engineers, 1967
10. B. Avitzur, "Strain Hardening and Strain Rate Effects in Plastic Flow through Conical Converging Dies," Paper 66-Prod-17, American Society of Mechanical Engineers, 1966
11. R. Hill, On the Inhomogeneous Deformation of a Plastic Lamina in a Compression Test, *Philos. Mag.,* Vol 41, 1950, p 733
12. J.F. Nye, Experiments on the Plastic Compression of a Block between Rough Plates, *J. Appl. Mech. (Trans. ASME),* Vol 19, 1952, p 337
13. J.J. Shah and H.A. Kuhn, An Empirical Formula for Workability Limits in Cold Upsetting and Bolt Heading, *Proceedings of 13th NAMRC,* Society of Mechanical Engineers, 1985
14. C.L. Downey and H.A. Kuhn, Application of a Forming Limit Criterion to Design of Preforms for Powder Forging, *J. Eng. Mater. Technol. (Trans. ASME),* Vol 97H, 1975, p 121
15. H.A. Kuhn, Deformation Processing of Sintered Powder Materials, *Powder Metallurgy Processing,* H.A. Kuhn and A. Lawley, Ed., Academic Press, 1978, p 99
16. Z. Zimerman, H. Darlington, and E.H. Kottcamp, Jr., Selection of Operating Parameters to Prevent Central Bursting during Cold Extrusion, *Mechanical Working and Steel Processing,* The Metallurgical Society, 1970, p 405